MNRAS **544**, 1412–1431 (2025) Advance Access publication 2025 October 9

# The JWST Emission Line Survey (JELS): the sizes and merger fraction of star-forming galaxies during the Epoch of Reionization

H. M. O. Stephenson<sup>®</sup>, <sup>1\*</sup> J. P. Stott<sup>®</sup>, <sup>1\*</sup> C. A. Pirie<sup>®</sup>, <sup>2</sup> K. J. Duncan<sup>®</sup>, <sup>2</sup> D. J. McLeod<sup>®</sup>, <sup>2</sup> P. N. Best, <sup>2</sup> M. Brinch, <sup>3</sup> M. Clausen, <sup>2</sup> R. K. Cochrane<sup>®</sup>, <sup>2,4,5</sup> J. S. Dunlop, <sup>2</sup> S. R. Flury<sup>®</sup>, <sup>2</sup> J. E. Geach<sup>®</sup>, <sup>6</sup> C. L. Hale<sup>®</sup>, <sup>7</sup> E. Ibar, <sup>3,8</sup> Zefeng Li<sup>®</sup>, <sup>9</sup> J. Matthee<sup>®</sup>, <sup>10</sup> R. J. McLure, <sup>2</sup> L. Ossa-Fuentes, <sup>3</sup> A. L. Patrick, <sup>2</sup> D. Sobral<sup>11,12</sup> and A. M. Swinbank<sup>®</sup>

Accepted 2025 October 2. Received 2025 September 8; in original form 2025 July 7

# ABSTRACT

We used observations from the *JWST* Emission Line Survey (JELS) to measure the half-light radii ( $r_e$ ) of 23 H $\alpha$ -emitting starforming (SF) galaxies at z=6.1 in the PRIMER/COSMOS field. Galaxy sizes were measured in *JWST* near-infrared camera observations in rest-frame H $\alpha$  (tracing recent star formation) with the F466N and F470N narrow-band filters from JELS, and compared against rest-R- and V-band (tracing established stellar populations) and near-ultraviolet sizes. We find a size–stellar mass ( $r_e-M_*$ ) relationship with a slope that is consistent with literature values at lower redshifts, though offset to lower sizes. We observe a large scatter in  $r_e$  at low stellar mass ( $M_* < 10^{8.4} \, \rm M_{\odot}$ ) which we believe is the result of bursty star formation histories (SFHs) of SF galaxies at the Epoch of Reionization (EoR). We find that the stellar and ionized gas components are similar in size at z=6.1. The evidence of already-established stellar components in these H $\alpha$  emitters (HAEs) indicates previous episodes of star formation have occurred. As such, following other JELS studies finding our HAEs are undergoing a current burst of star formation, we believe our results indicate that SF galaxies at the end of the EoR have already experienced a bursty SFH. From our  $r_e-M_*$  relationship, we find  $r_{e, \rm F444W}=0.76\pm0.46\,\rm kpc$  for fixed stellar mass  $M_*=10^{9.25}\,\rm M_{\odot}$ , which is in agreement with other observations and simulations of SF galaxies in the literature. We find a close-pair (major) merger fraction of ( $f_{\rm maj.\ merger}=0.44\pm0.22$ )  $f_{\rm merger}=0.43\pm0.11$  for galaxy separations  $d\lesssim 25\,\rm kpc$ , which is in agreement with other  $z\approx 6$  studies.

**Key words:** galaxies: evolution – galaxies: high-redshift – galaxies: starburst – galaxies: star formation.

# 1 INTRODUCTION

The redshift evolution of the basic physical properties of galaxies, such as their size, stellar mass  $(M_*)$ , luminosity, and morphology provide vital constraints for models of galaxy formation. Additionally, how these properties change with respect to each other can constrain the evolutionary tracks that galaxies follow. One example is the size distribution of galaxies as a function of their stellar mass. Galaxy size is often measured in units of 'effective' or 'half-light'

\*E-mail: h.stephenson@lancaster.ac.uk (HMOS); j.p.stott@lancaster.ac.uk (JPS)

radius  $(r_e)$ , defined as the radius in which half of a galaxy's light is contained.  $r_e$  can range from  $\approx 0.1$  (e.g. Y. Ono et al. 2023) to  $\gtrsim 10$  kpc (e.g. R. Kawamata et al. 2015; B. T. Dullo, A. W. Graham & J. H. Knapen 2017). The distribution and evolution of  $r_e$  can be used to infer properties of the host dark matter (DM) halo, including its virial radius (H. J. Mo, S. Mao & S. D. M. White 1998; A. A. Dutton et al. 2007; J. Fu et al. 2010), spin or angular momentum (J. S. Bullock et al. 2001; A. A. Dutton 2009), and merger history (T. Naab, P. H. Johansson & J. P. Ostriker 2009; J. R. Ownsworth et al. 2014).

There is strong evidence that galaxy sizes correlate with stellar mass such that higher mass galaxies have a larger  $r_e$  (the size–mass relationship;  $r_e - M_*$ ). In their influential work, S. Shen et al. (2003)

<sup>&</sup>lt;sup>1</sup>Department of Physics, Lancaster University, Lancaster LA1 4YB, UK

<sup>&</sup>lt;sup>2</sup>Institute for Astronomy, University of Edinburgh, Royal Observatory, Blackford Hill, Edinburgh EH9 3HJ, UK

<sup>&</sup>lt;sup>3</sup>Instituto de Física y Astronomía, Universidad de Valparaíso, Avda., Gran Bretaña 1111, Valparaíso, Chile

<sup>&</sup>lt;sup>4</sup> Jodrell Bank Centre for Astrophysics, University of Manchester, Oxford Road, Manchester M13 9PL, UK

<sup>&</sup>lt;sup>5</sup>Department of Astronomy, Columbia University, New York, NY 10027, USA

<sup>&</sup>lt;sup>6</sup>Centre for Astrophysics Research, School of Physics, Engineering and Computer Science, University of Hertfordshire, College Lane, Hatfield, AL10 9AB, UK

<sup>&</sup>lt;sup>7</sup>Astrophysics, Department of Physics, University of Oxford, Denys Wilkinson Building, Keble Road, Oxford OX1 3RH, UK

<sup>&</sup>lt;sup>8</sup>Millennium Nucleus for Galaxies (MINGAL), Valparaíso, Chile

<sup>&</sup>lt;sup>9</sup>Centre for Extragalactic Astronomy, Department of Physics, Durham University, South Road, Durham DH1 3LE, UK

<sup>&</sup>lt;sup>10</sup>Institute of Science and Technology Austria (ISTA), Am Campus 1, A-3400 Klosterneuburg, Austria

<sup>&</sup>lt;sup>11</sup>Departamento de Física, Faculdade de Cièncias, Universidade de Lisboa, Edifício C8, Campo Grande, P-1749-016 Lisbon, Portugal

<sup>&</sup>lt;sup>12</sup>BNP Paribas Corporate & Institutional Banking, Torre Ocidente Rua Galileu Galilei, P-1500-392 Lisbon, Portugal

studied the  $r_e$  distributions of  $\approx$ 140 000 galaxies in the Sloan Digital Sky Survey (SDSS; D. G. York et al. 2000; C. Stoughton et al. 2002) as a function of stellar mass and luminosity and found a clear correlation with both. They also found that both relations are significantly steeper for early-type galaxies than late-type galaxies, the latter of which has a characteristic stellar mass in the local Universe  $(M_{*,0} = 10^{10.6} \,\mathrm{M_\odot})$  above which the slope steepens but remains shallower than that of early-type galaxies. A. van der Wel et al. (2014) extended the analysis of the mass-size relation out to higher redshifts, covering  $0 \le z \le 3$  by making use of *Hubble Space* Telescope (HST) data from the 3D-HST survey (G. B. Brammer et al. 2012) and the Cosmic Assembly Near-infrared Deep Extragalactic Legacy Survey (CANDELS; N. A. Grogin et al. 2011; A. M. Koekemoer et al. 2011). The results of A. van der Wel et al. (2014) are in qualitative agreement with S. Shen et al. (2003) such that the slope of the  $r_e - M_*$  relation is shallower for late-type galaxies, though they see a flattening in the slope of early-type galaxies at  $M_* \lesssim 10^{10} \,\mathrm{M_\odot}$ . Many studies have measured  $r_e - M_*$  relations at a range of redshifts (0 < z < 5; E. Daddi et al. 2005; I. Trujillo et al. 2006, 2007; J. P. Stott et al. 2011, 2013a; R. Lange et al. 2015; A. Paulino-Afonso et al. 2017; A. L. Faisst et al. 2017; L. Mowla et al. 2019a; L. A. Mowla et al. 2019b). More recently, studies have utilized the high resolution of JWST (J. P. Gardner et al. 2006; J. Rigby et al. 2023) in the near-infrared (NIR) to study the structural properties of galaxies in the rest-frame optical at  $z \ge 3$  including sizes (K. A. Suess et al. 2022; Y. Ono et al. 2023; K. Ormerod et al. 2023; N. Allen et al. 2025; Z. Ji et al. 2024a; M. Martorano et al. 2024; R. G. Varadaraj et al. 2024; E. Ward et al. 2024; T. B. Miller et al. 2025; L. Westcott et al. 2025), resolved star formation (Z. Ji et al. 2024b; J. Li et al. 2024; J. Matharu et al. 2024; T. Morishita et al. 2024), and morphology (K. Ito et al. 2024; Y. Ono et al. 2024, 2025; J. Vega-Ferrero et al. 2024).

As mentioned above, there has been a clear redshift evolution of  $r_e$  and the  $r_e-M_*$  relationship. A. van der Wel et al. (2014) found that their  $r_e$  measurements at  $z\sim 0$  are consistent with those of SDSS galaxies in S. Shen et al. (2003) and Y. Guo et al. (2009) (after accounting for systematic differences in their respective methods; see A. van der Wel et al. 2014), but observed an increasing offset from the local  $r_e-M_*$  relation for higher redshift galaxies. The power law that they use to describe the redshift evolution of galaxy sizes is of the form

$$\frac{r_e}{\text{kpc}} = B(1+z)^{\beta},\tag{1}$$

where B is the intercept and  $\beta$  is the power-law slope. Equation (1) is used as standard in the literature to describe the redshift evolution of  $r_e$ , typically for some characteristic stellar mass (J. P. Stott et al. 2013a; T. Shibuya, M. Ouchi & Y. Harikane 2015; A. Paulino-Afonso et al. 2017; S. E. Cutler et al. 2022; W. Sun et al. 2024; A. van der Wel et al. 2024). Specifically, A. van der Wel et al. (2014) find that for a fixed stellar mass of  $10^{10.75}\,\mathrm{M}_{\odot}$ , the sizes of late- and early-type galaxies evolve as  $r_e \propto (1+z)^{-0.72}$  and  $r_e \propto (1+z)^{-1.24}$ respectively. These results reflect an  $\approx 3.7$  kpc ( $\approx 55$  per cent) and  $\approx$  $3.2 \,\mathrm{kpc}$  ( $\approx 74 \,\mathrm{per}$  cent) decrease in  $r_e$ , respectively, between z < 0.5and z = 2.5 - 3. Using JWST data from The Cosmic Evolution Early Release Survey (CEERS; S. L. Finkelstein et al. 2023; M. B. Bagley et al. 2023) and HST data from CANDELS, E. Ward et al. (2024) found that the average  $r_e$  decreased further out to z = 5.5. Their power-law slope of  $\beta = -0.67 \pm 0.07$  for a characteristic mass of  $\approx 10^{10.7}\,M_{\odot}$  is also consistent with that of A. van der Wel et al. (2014). It is crucial to extend analysis of galaxy sizes to even higher redshifts, and for homogeneously selected populations, in order to

constrain this power law further and to shed new light on the first era of galaxy formation.

In order to disentangle the contributions of active star formation from the longer term, in-situ star formation history (SFH) on the size evolution discussed above, one must use star formation rate (SFR) indicators that are distinct to both, as well as high spatial resolution images to resolve active star-forming (SF) regions. The  $H\alpha$  (6563 Å) emission line is one of the most frequently used SFR indicators for recent star formation in a galaxy (R. C. Kennicutt 1998; D. K. Erb et al. 2006; D. Sobral et al. 2013; Y. Terao et al. 2022; A. Covelo-Paz et al. 2025). This is because it traces the ionized gas emission resulting from the recombination of hydrogen surrounding the most massive stars (C.-N. Hao et al. 2011b; E. J. Murphy et al. 2011), which typically only live for  $\leq 10 \,\mathrm{Myr}$  (S. Ekström et al. 2012). The rest-frame ultraviolet (UV) or near-UV (NUV) continuum of a galaxy can also be used to trace star formation, but on longer time-scales ( $\sim 10 - 200 \, \mathrm{Myr}$ ) as it traces the photons emitted directly from the photospheres of stars upwards of several solar masses. For a comprehensive review of SFR indicators and the populations they trace, see R. C. Kennicutt & N. J. Evans (2012; also P. Madau & M. Dickinson 2014; S. F. Sánchez 2020; E. Schinnerer & A. Leroy 2024). Typically, the UV continuum has been used to infer the SFR of galaxies at  $z \ge 2$  as its wavelength gets redshifted into optical bands (T. K. Wyder et al. 2005; R. J. Bouwens et al. 2012a, b, 2015; P. A. Oesch et al. 2018; Y. Harikane et al. 2023), whereas H $\alpha$  is shifted further into IR bands which are more difficult to observe with ground based instruments. However, UV measurements are extremely sensitive to dust attenuation (e.g. D. Calzetti, A. L. Kinney & T. Storchi-Bergmann 1994; J. S. Dunlop et al. 2017; R. Bouwens et al. 2020; A. Traina et al. 2024). and there is evidence that the effects of dust continue to impact observations out to the Epoch of Reionization (EoR; C. Gruppioni et al. 2020; R. A. A. Bowler et al. 2022; H. S. B. Algera et al. 2023; J. A. Zavala et al. 2023). Moreover, while there exist dust attenuation calibrations that aim to correct for these issues (e.g. D. Calzetti et al. 2000; S. Salim et al. 2007), these depend heavily on assumptions of the UV continuum slope, intrinsic colours, and the choice of dust extinction curve which may impact the measured properties of these selected objects (J. Walcher et al. 2011; P. Arrabal Haro et al. 2023).

The benefit of the H $\alpha$  emission line is that it is less affected by dust attenuation, which relieves these issues (though we note that the extinction in the nebula regions is more uncertain at high-z; N. A. Reddy et al. 2020, 2025). With JWST able to access H $\alpha$  at  $z \gtrsim 2.5$ , combined with its high-resolution imaging, we are now able to probe the physical properties of samples of SF galaxies at earlier times than before. Some studies are already showcasing the ability to probe star formation using H $\alpha$  out to  $z \sim 3.7 - 6.5$  using grism spectroscopy to select on H $\alpha$  (J. Matharu et al. 2023; E. Nelson et al. 2024; A. Covelo-Paz et al. 2025). Another approach is to use narrow-band (NB) imaging selection on  $H\alpha$  to look for SF galaxies, as this also provides a selection based on the strength of the emission line. A key advantage of NB imaging is that it mitigates the selection effects that can arise from slitless spectroscopy (such as source blending, or preferentially strong Lyman breaks) and, when combined with broadband (BB) photometry, provides a much narrower redshift range that sources can lie within. Additionally, it also provides a direct image without needing to reconstruct one from the slitless spectroscopy. This method was notably used by the Hi-Z Emission Line Survey (HiZELS; J. E. Geach et al. 2008; D. Sobral et al. 2009, 2013) which utilized the Wide Field Camera (M. Casali et al. 2007) on the United Kingdom Infrared Telescope to significantly expand the volume of previous NB imaging surveys (e.g. D. Thompson, F. Mannucci & S. V. W. Beckwith 1996; A. F. M. Moorwood et al. 2000). As a result of the NB imaging selection of HiZELS, many studies were able to measure the properties of homogeneously selected  $H\alpha$  emitters (HAEs) out to z=2.23 (D. Sobral et al. 2010; T. Garn et al. 2010; A. M. Swinbank et al. 2012a, b; D. Sobral et al. 2012, 2013; J. P. Stott et al. 2013b; I. Oteo et al. 2015; D. Sobral et al. 2016; R. K. Cochrane et al. 2017, 2018; C. Cheng et al. 2020; R. K. Cochrane et al. 2021), including  $r_e$  measurements (J. P. Stott et al. 2013a; A. Paulino-Afonso et al. 2017; A. Naufal et al. 2023).

In this paper, we use data from the JWST Emission Line Survey (JELS; GO no. 2321; PI: Philip Best; see K. J. Duncan et al. 2025; C. A. Pirie et al. 2025) to probe the  $r_e$  properties of 23 z = 6.1 SF galaxies in the first H $\alpha$ -selected sample of HAEs from NB imaging at the EoR. We combine the JELS observations with anicillary multiwavelength data from the JWST Cycle 1 Observer Treasury Program 'Public Release IMaging for Extragalactic Research' survey (PRIMER; PI Dunlop, GO no. 1837). We primarily use JWST/NIRCam long-wavelength (LW) channel observations in JELS F466N, JELS F470N NB, and PRIMER F444W BB filters to study the rest-frame R-band Sérsic light profiles (J. L. Sérsic 1963, 1968) of HAEs at the EoR, taking advantage of the image resolution JWST provides at  $\lambda \approx 3.8 - 5 \,\mu\text{m}$ . This allows us to probe both active star formation and older stellar populations at z = 6.1. In addition to rest-R-band sizes, we also measure the light profiles in PRIMER F277W (rest-NUV) and PRIMER F356W (rest-V-band). Our measured  $r_e$  values are then compared to both observations and simulations. We also measure the size ratio of the SF component (traced by the ionized gas from the H $\alpha$  emission) and the stellar continuum to infer how EoR HAEs have evolved over the preceding 1 Gvr

This paper is arranged as follows. In Section 2, we summarize the JELS survey and photometric catalogue. We explain how we determine our final sample of HAEs in Section 2.1. In Section 3, we describe the methods used to fit galaxy sizes in different wavebands. We outline key results in Section 4, and discuss their implications in Section 5. We summarize our conclusions in Section 6.

A standard Lambda-cold dark matter cosmology model is assumed with values  $\Omega_{\Lambda} = 0.7$ ,  $\Omega_m = 0.3$ , and  $H_0 = 70 \, \mathrm{km s^{-1} M^{-1} pc}$ . Any magnitudes stated are presented using the AB system (J. B. Oke & J. E. Gunn 1983). All results and comparisons to the literature in this paper assume a G. Chabrier (2003) initial mass function (IMF).

# 2 JELS DATA

The JELS survey is described in full by K. J. Duncan et al. (2025) and C. A. Pirie et al. (2025). Here, we will summarize the key details that are relevant for our work.

The primary goal of JELS is to provide a homogeneously selected catalogue of  $H\alpha$ -selected galaxies at the EoR from the Cosmological Evolution Survey (COSMOS) field (N. Scoville et al. 2007a, b). In this context, 'homoegeneously selected' refers to the fact galaxies are identified solely based on their  $H\alpha$  emission-line strength, providing a uniform tracer of star formation and avoiding biases introduced by continuum- or colour-based selection methods. This is, in effect, a selection on SFR, though we note here the catalogue described in this section is complete in stellar mass to  $\approx 10^{8.2}\,{\rm M}_{\odot}$ . This selection is achieved by employing the F466N and F470N NB filters in the *JWST/*NIRCam LW channels, with pivot wavelengths of

 $\lambda_{\rm pivot} = 4.654 \,\mu{\rm m}$  (effective width  $W_{\rm eff} = 0.0535 \,\mu{\rm m}$ ) and  $\lambda_{\rm pivot} =$  $4.707 \,\mu\text{m}$  ( $W_{\text{eff}} = 0.0510 \,\mu\text{m}$ ) respectively. These two filters centre on  $z \approx 6.09$  and  $\approx 6.17$  for the H $\alpha$  emission line which allows for line emitters to be selected through difference imaging in a selection volume of  $\sim 2.4 \times 10^4 \, \text{Mpc}^3$ . In addition, the NB observations from JELS are designed to overlap with multiwavelength observations from CANDELS (N. A. Grogin et al. 2011; A. M. Koekemoer et al. 2011; G. B. Brammer et al. 2012; H. Teplitz 2018) and, more crucially, with the JWST Cycle 1 Observer Treasury Program PRIMER survey (PI Dunlop, GO no. 1837). Specifically, LW BB observations in the F444W filter ( $\lambda_{\rm pivot} = 4.4043 \, \mu \rm m$ ;  $W_{\rm eff} = 1.0676 \, \mu \rm m$ ) from PRIMER - with a wavelength range that covers F466N and F470N – allow for this NB excess selection at  $\sim 4.7\,\mu m.$  In this work, we also make use of PRIMER observations in F277W ( $\lambda_{pivot}$  =  $2.7617 \, \mu m; \ W_{eff} = 0.6615 \, \mu m) \ and \ F356W \ (\lambda_{pivot} = 3.5684 \, \mu m;$  $W_{\rm eff} = 0.7239 \,\mu \rm m)$  for rest-NUV and rest-V-band measurements respectively. The resulting deep, multiwavelength coverage has enabled robust photometry for spectral energy distribution (SED) fitting to constrain the SFH of the HAEs. The SED fitting for our HAEs was performed by C. A. Pirie et al. (2025) using the BAGPIPES spectral fitting code (A. C. Carnall et al. 2018). They use BPASS (J. J. Eldridge et al. 2017; E. R. Stanway & J. J. Eldridge 2018) for their stellar population synthesis model, and the CLOUDY photoionization code (G. J. Ferland et al. 2017) for nebular emissionline computation. They assume a S. Salim, M. Boquien & J. C. Lee (2018) dust attenuation model and the continuity non-parametric SFH model from J. Leja et al. (2019). We refer the reader to table 8 of C. A. Pirie et al. (2025) for details on the models and

Overall, the JELS survey has continuous coverage over  $\sim$  63 arcmin² area of the COSMOS field (see fig. 3 of K. J. Duncan et al. 2025) with the final images homogenized to a common point spread function (PSF) with a resolution of  $0.03 \times 0.03$  arcsec² pixel $^{-1}$ .

We note here that the science conducted in this paper is based on the initial versions of the JELS imaging products, referred to as v0.8 images, also used in C. A. Pirie et al. (2025). The newer v1.0 images incorporate re-observations taken in 2024 November to better mitigate scattered light issues and use an updated version of the *JWST* pipeline for image reduction. We refer the reader to appendix A of K. J. Duncan et al. (2025) for details on the differences between the v0.8 images used here and the updated v1.0 images. Throughout this work, all references to source IDs are referring to their JELS v0.8 catalogue value and may not correspond to subsequent revisions of the catalogue.

# 2.1 Sample selection

To analyse the structural properties of SF galaxies at the EoR, we derive our own sample from the multiwavelength JELS v0.8 catalogues that are described in detail by C. A. Pirie et al. (2025), specifically their sections 3 and 4 where the method for identifying NB excess emitters from multiwavelength detections is outlined. Briefly, their selection is based on significant NB excess relative to either the overlapping PRIMER F444W BB or neighbouring NB filter, combined with photo-z cuts around  $z \sim 6.1$ , with additional visual inspection to remove residual contamination. Following this, they finalize a catalogue of 35 HAEs (30 F466N sources; 5 F470N sources). We refer to the C. A. Pirie et al. (2025) catalogue as the 'parent' catalogue in this paper, and it is from this that we determine the sample used for the analysis in this work.

In order to accurately measure  $r_e$ , we need a sample that we are able to reliably measure the Sérsic profiles of. Therefore, we removed

<sup>&</sup>lt;sup>1</sup>https://primer-jwst.github.io

sources from the parent catalogue of C. A. Pirie et al. (2025) that had some additional complications which made them difficult/impossible to reliably model. Here, we will outline which sources were removed, reiterating that the IDs refer to the JELS v0.8 catalogue. Sources 2768 and 7810 (both F466N selected) were removed because light profile fits in both NB and F444W images strongly preferred a PSF model over a Sérsic model (based on the  $\chi^2$  outputs of the GALFIT model; see Section 3.1), indicative of a point source dominating any galactic emission; 12164 (F466N) was removed because a PSF model was strongly preferred in the F444W image (see Section 3.1) meaning point source emission is likely dominating; 4453 and 4457 (both F466N) were removed as they appear to be a merging system (see Section 4.4) that is too faint to individually model in the F444W image; 10983 (F466N) was removed because, despite being an isolated source in the NB image, it appears to be part of a three-way merging system in F444W which made it difficult to isolate when modelling. Finally, a number of HAEs were too faint in F444W to accurately model. From F466N detections, 5629 ( $\approx 28.7 \,\mathrm{mag}$ ),  $6501 \approx 28.8 \,\mathrm{mag}$ ,  $7147 \approx 29.3 \,\mathrm{mag}$ , and  $9123 \approx 28.7 \,\mathrm{mag}$  were removed, as well as 8033 ( $\approx 30.1 \,\mathrm{mag}$ ) and 15619 ( $\approx 28.8 \,\mathrm{mag}$ ) from F470N detections. See fig. A1 of C. A. Pirie et al. (2025) for multiwavelength imaging of all excess sources, including those we do not include in our final HAEs sample.

Following these removals, we obtain a sample of 23 H $\alpha$ -emitting SF galaxies at z=6.1 (20 detected in F466N; and 3 detected in F470N). These galaxies have a stellar mass range of  $M_*=10^{8.06-9.28}\,{\rm M}_\odot$  ( $M_{*,\rm median}=10^{8.30}\,{\rm M}_\odot$ ), and SFR range of SFR $_{\rm H}\alpha=1.03-14.22\,{\rm M}_\odot\,{\rm yr}^{-1}$  (median SFR $_{\rm H}\alpha,{\rm median}=2.73\,{\rm M}_\odot\,{\rm yr}^{-1}$ ). Stellar masses and SFRs are derived in C. A. Pirie et al. (2025), where the latter is determined using the H $\alpha$  SFR relation in R. L. Theios et al. (2019). We note SFR values derived from H $\alpha$  are consistent with the 10 Myr SFR output from SED fitting. All stellar mass and SFR values in C. A. Pirie et al. (2025) are converted here to a G. Chabrier (2003) IMF.

The parent catalogue is representative of HAEs at z=6.1 in terms of H $\alpha$  equivalent width (EW; see fig. 11 of C. A. Pirie et al. 2025), with an EW limit well below the SF galaxy population at this redshift (see R. Endsley et al. 2024). Our final sample of 23 HAEs is similarly representative in EW, and we note that our final sample is also complete in stellar mass down to  $\approx 10^{8.2}\,\mathrm{M}_{\odot}$ .

# 3 SÉRSIC MODELLING

To measure the Sérsic light profiles (J. L. Sérsic 1963, 1968) of our sources, we use GALFIT<sup>2</sup> version 3.0.7d4 (C. Y. Peng et al. 2002, 2010) – a non-linear least-squares fitting algorithm designed for 2D parametric galaxy fitting. GALFIT uses a Levenberg–Marquardt algorithm to find an optimum solution when modelling the light profile of a source for a given input image. This best-fitting solution is determined via a reduced chi-squared ( $\chi^2_{\nu}$ ) method, whereby GALFIT iterates over a large number of possible models by adjusting the input parameters until  $\chi^2$  is minimized.  $\chi^2_{\nu}$  describes the goodness of fit of the output model and is determined by

$$\chi_{\nu}^{2} = \frac{1}{N_{\text{DOF}}} \sum_{r=1}^{nx} \sum_{y=1}^{ny} \frac{(f_{\text{data}}(x, y) - f_{\text{model}}(x, y))^{2}}{\sigma(x, y)^{2}},$$
 (2)

where  $N_{\rm DOF}$  is the number of degrees of freedom (DOF),  $f_{\rm data}(x, y)$  represents the data image supplied to GALFIT,  $f_{\rm model}(x, y)$  represents

the model image that GALFIT outputs following the least-squares fitting, and  $\sigma(x, y)$  represents the sigma image fed to GALFIT. The sigma image is the relative error of the flux at each position (x, y) within the data image. This is summed over all x and y pixels, where nx and ny are the x and y dimensions, respectively, of the data and model images.

We fit a Sérsic model of the form

$$\Sigma(r) = \Sigma_e \exp\left\{-b_n \left[ \left(\frac{r}{r_e}\right)^{1/n} - 1 \right] \right\},\tag{3}$$

where  $\Sigma(r)$  is the pixel surface brightness at radius r from the centre of a source,  $r_e$  is the half-light radius of the source, and  $\Sigma_e$  is the pixel surface brightness at  $r_e$ . The Sérsic index of the model, n, determines the overall shape of the light profile and  $b_n$  is a dimensionless scale factor that is dependent on n (see L. Ciotti & G. Bertin 1999 for full explanation and asymptotic expansion). In general, late-type galaxies follow a Sérsic light profile with  $n \lesssim 2.5$  (shallow inner profile which truncates more sharply at large r; J. L. Sérsic 1968; L. S. Kelvin et al. 2012) and early-type galaxies follow a profile where  $n \gtrsim 2.5$  (sharply decreasing inner profile with r but extended wing at large r; N. Caon, M. Capaccioli & M. D'Onofrio 1993). The most commonly used Sérsic indices are n=1 which describes a purely exponential profile suitable for galactic discs (K. C. Freeman 1970), and n=4 which gives a de Vaucouleurs profile (G. de Vaucouleurs 1948) suitable for bright elliptical galaxies.

# 3.1 Fitting with GALFIT

For our HAEs, we fit a single-component Sérsic profile in all the images we model. We particularly focus on results from the detected JELS F466N and F470N images and the corresponding PRIMER F444W image (equivalent to rest-R-band). This is to measure  $r_e$  of both the H $\alpha$ -selected SF component and the emission from the stellar population respectively. However, we also follow the procedures in this section for the PRIMER F277W and PRIMER F356W images for rest-NUV and rest-V-band sizes, respectively. From this, we can then assess how our results at z=6.1 compare to sizes in the literature, including other  $r_e-M_*$  relations. We can also directly compare the NB and F444W sizes to draw conclusions about how SF galaxies are evolving at the EoR (see Section 4.2). The steps we take to model our sources are as follows:

(i) First, we create  $100 \times 100 \, \mathrm{pixel^2}$  ( $3 \times 3 \, \mathrm{arcsec^2}$ ;  $\sim 17 \times 17 \, \mathrm{kpc^2}$ ) cutouts of each source centred on the corresponding right ascension (R.A.) and declination (Dec.) of the SEXTRACTOR (E. Bertin & S. Arnouts 1996) source coordinates in a given band. We do the same for the corresponding 'weights' map which is used to create the sigma image to be fed to GALFIT. This weights map has pixel values equal to  $1/(\sigma(x,y)^2)$  so, accordingly, these values are converted such that the sigma image pixel values are  $\sigma(x,y)$ . Such a relatively large area for the cutout image was decided in order for GALFIT to measure the sky background and confidently capture the wings of the PSF (see below). Any additional sources in the cutout, identified via SEXTRACTOR, are modelled separately so that their light is not accounted for in the selected source model.

(ii) As with all telescopes, JWST images have an intrinsic PSF that must be accounted for (M. D. Perrin et al. 2014; J. Rigby et al. 2023). We chose to use empirical  $100 \times 100$  pixel<sup>2</sup> PSFs described in detail by C. A. Pirie et al. (2025). In summary, these empirical, filter-dependent PSFs were generated by stacking bright and unsaturated stars in a given filter via a boostrapping method. These PSFs from C.

<sup>&</sup>lt;sup>2</sup>https://users.obs.carnegiescience.edu/peng/work/galfit/galfit.html

A. Pirie et al. (2025) are comparable to simulated PSFs<sup>3</sup> generated by WEBBPSF<sup>4</sup> (M. D. Perrin et al. 2014). The choice of PSF makes no significant difference to our results.

(iii) GALFIT requires a set of initial estimates to be provided for each of the fitted parameters. These are the centroid x and y coordinates of the source in pixel units; the integrated apparent magnitude in the chosen filter;  $r_e$  in pixel units; the Sérsic index n; the semiminor axis over semimajor axis radius ratio (axis ratio b/a = q, where q = 1 for a circle and q < 1 for an ellipse); and the position angle ( $\theta_{pa}$ ) of the major axis on the sky in degrees measured anticlockwise from north. Similar to previous studies, we use the SEXTRACTOR outputs for each of these parameters as our initial guess (e.g. A. van der Wel et al. 2012; L. A. Mowla et al. 2019b; J. S. Kartaltepe et al. 2023; K. Ormerod et al. 2023; L. Westcott et al. 2025), with the exception of the integrated magnitude as we used magnitudes derived from flux inside a 0.6 arcsec-diameter aperture centred on each source to be consistent with C. A. Pirie et al. (2025).

(iv) The nature of these observations means that these distant galaxies tend to be very small on the image, causing GALFIT to often get stuck in local minima that produce unrealistic output parameters. Additionally, GALFIT will fail if it cannot produce a physical solution (C. Y. Peng et al. 2010). To avoid these outcomes, we apply constraints to bound each parameter to be between certain values. These constraints are as follows: the centroid coordinates are allowed to vary  $\pm 5$  pixels from the input values in both x and y; the integrated magnitude is allowed to vary  $\pm 2$  mag from the input value;  $r_e$  is constrained to  $0.1 \le r_e \le 100$  pixels; the axis ratio is constrained to  $0.2 \le q \le 1$ ; and  $\theta_{pa}$  is allowed to vary  $\pm 20^{\circ}$  from the input values. Each of these constraints are applied to all images. For the Sérsic index n, we initially took two approaches. When modelling in the NB images (F466N and F470N), n is fixed at n = 1since the light profile of any ionized gas emission is expected to be disc-like (e.g. E. J. Nelson et al. 2013), and our size measurements are consistent regardless of a fixed or free Sérsic index fit (see the right panel of Fig. A1). SF galaxies at high-z that appear more prolate or oblate in shape have also been shown to have Sérsic indices of  $n \sim 1$ (e.g. V. Pandya et al. 2024). For the BB images (F277W, F356W, and F444W), we produced two sets of results. One in which n is again fixed at n = 1, and another set where we allowed n to take values  $0.2 \le n \le 8$ . The measurements of  $r_e$  in the BB images using both methods are in agreement (see the left panel of Fig. A1 for results in F444W), and so we chose to fix n = 1 for all of our models for ease of interpretation. When the Sérsic index was left as a free parameter, we find  $n_{\rm F444W, median} \sim 1.5$ .

(v) It is well documented that GALFIT underestimates the uncertainties of each outputted parameter (B. Häußler et al. 2007, 2013). Recently, E. Ward et al. (2024) addressed this by following steps from A. van der Wel et al. (2012) to recalculate the uncertainty on  $r_e$  compared to the reported value from GALFIT. They found that their new relative  $r_e$  errors for their *JWST* images were  $\lesssim$  15 per cent, similar to those reported in other studies (A. van der Wel et al. 2012; K. V. Nedkova et al. 2021). In light of their findings, we set our uncertainties in  $r_e$  to be at least 25 per cent of the GALFIT output to be conservative. This is an average factor increase in uncertainty of  $\sim$  3.6 from the GALFIT output. We refer the reader to Section 3.1.1 for detailed analysis of  $r_e$  recovery in GALFIT from known values.

We show six examples of our GALFIT models in Fig. 1. The sensitivity of GALFIT is alleviated by the constraints described above but following visual inspection, the input centroid coordinates had to be manually adjusted for a small number of models to be closer to the observed centre of the galaxy. None of the adjustments left the SEXTRACTOR source coordinates outside of the range of estimates GALFIT could take (i.e. manual input was never more than 5 pixels from the initial input) but were necessary adjustments for GALFIT to avoid unphysical local minima in its solution, which we define as being any solution that has an output  $r_e = 0.1$  or 100 pixels.

We note that there are potential degeneracies with modelling Sérsic light profiles with GALFIT, particularly that  $r_e$  and the Sérsic index n may be not be independent (see A. W. Graham & S. P. Driver 2005 for a detailed discussion). This could be a particularly pressing issue for our fixed n=1 sizes, though lack of posterior distribution outputs from GALFIT make this difficult to quantify directly (C. Y. Peng et al. 2010; B. Häußler et al. 2007, 2013). However, we show in Appendix A that our sizes are consistent when using either a free Sérsic or fixed n=1 suggesting that the possible limitations of GALFIT do not significantly impact our results.

#### 3.1.1 Recovering known sizes with GALFIT

In Section 3.1, we discussed the uncertainty estimations of GALFIT and how it typically underestimates them (see B. Häußler et al. 2007, 2013; also A. van der Wel et al. 2012). There is also evidence that for faint, compact objects, GALFIT begins to overestimate the sizes of galaxies. For example, R. Davari et al. (2014) found that GALFIT can overestimate the sizes by as much as 20 per cent when fitting a single Sérsic profile to multicomponent, early-type galaxies (see also M. Mosleh, R. J. Williams & M. Franx 2013; A. Meert, V. Vikram & M. Bernardi 2013; J.-H. Wang et al. 2024a), though they note galaxies at high-z like those we study in this paper are not as prone to those specific issues. Moreover, our HAEs are likely late-type galaxies given their selection criteria and SFR (C. A. Pirie et al. 2025).

Despite this, we decided to probe GALFIT's ability to recover accurate  $r_e$  measurements by measuring the Sérsic profiles of model galaxies in 33 000 mock images in F444W with similar properties to those of our sample of HAEs. In total, we created 330 n = 1 model galaxies using GALFIT with properties in the range  $m_{\rm F444W} = 24$  – 29 mag,  $r_{e,\text{model}} \approx 0.4 - 1.8 \,\text{kpc}$ , and b/a = 0.2 - 1.0. Each mock galaxy was then placed in 100 random sky cutouts of the full PRIMER F444W image. These sky cutouts were created by ensuring that no SEXTRACTOR-detected sources were within  $\sqrt{100^2 + 100^2} \approx 141$ pixels of the centre of the cutout. We then ran GALFIT on these model galaxies with sky backgrounds following the steps in Section 3.1 with n kept fixed at n = 1, as well as fits where it is left as a free parameter for a total of 66 000 fits. We then bin the results on the model F444W magnitude and  $r_{e, model}$ , with each bin containing 600 outputs. We then remove any catastrophic fitting errors which we define here as those that run up against the  $r_e$  constraint boundaries (or n boundaries for when n is a free parameter). In other words, we remove any fit that produces a fit with  $r_e = 0.1$  or 100 pixels (n = 0.2or 8 for the free Sérsic index fits). The number of catastrophic errors varied depending on model values, reaching as high as 67 per cent (402/600) for models with an apparent F444W magnitude of 29 mag and  $r_e \approx 1.4$  kpc. From the remaining fits, we then determine the median recovered  $r_e$  ( $r_{e,median}$ ) in each bin and the standard

Fig. 2 shows the  $r_{e,\text{median}}/r_{e,\text{model}}$  ratio (left axis) of fixed n=1 mock galaxies in 0.5-wide magnitude bins. The different coloured

psf-simulation-tool

<sup>&</sup>lt;sup>3</sup>https://jwst-docs.stsci.edu/jwst-near-infrared-camera/nircamperformance/nircam-point-spread-functions <sup>4</sup>https://www.stsci.edu/jwst/science-planning/proposal-planning-toolbox/

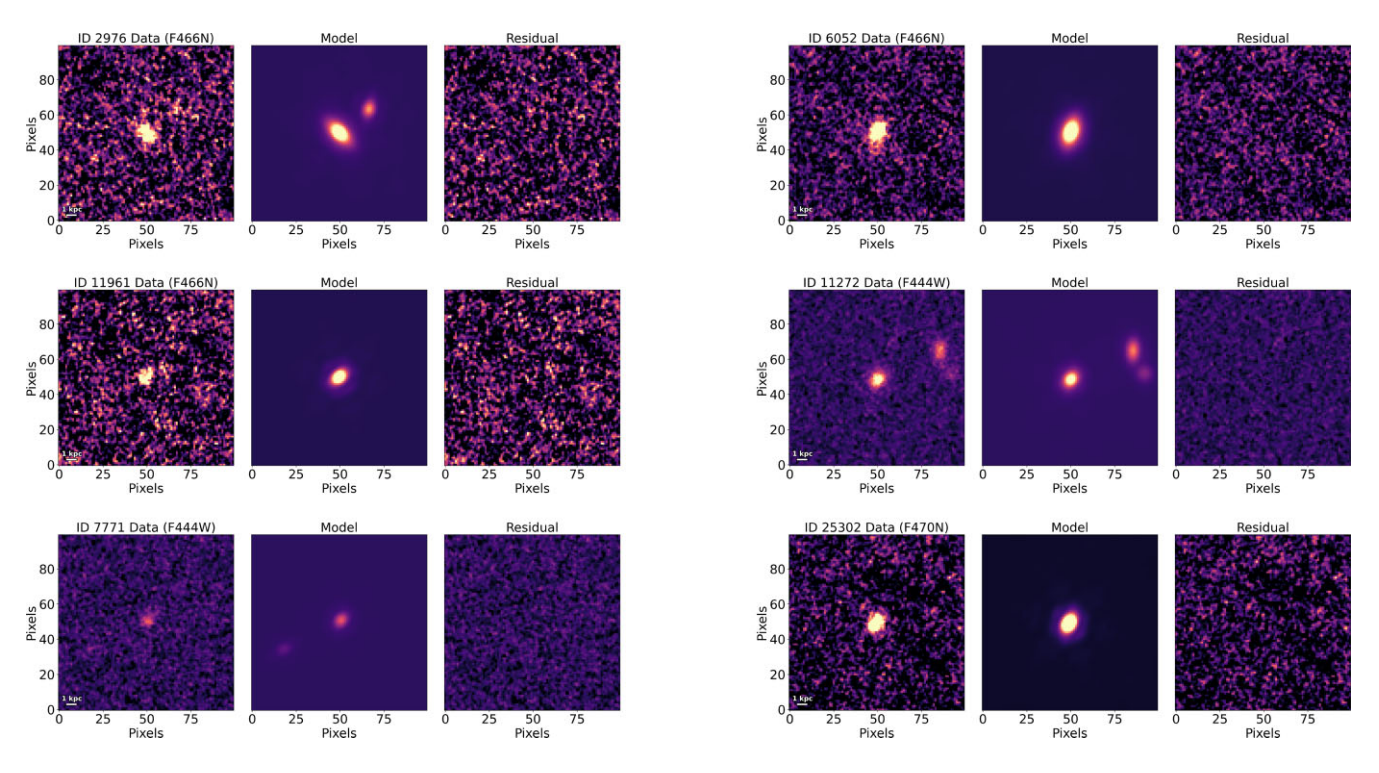
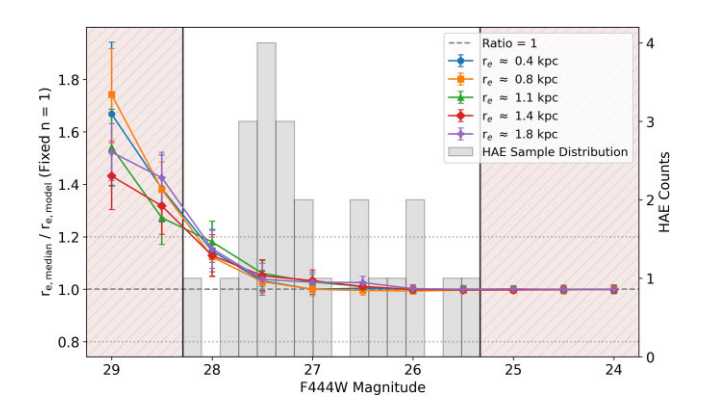


Figure 1. Example models for six HAEs in our sample. The left panels are the rest-frame *R*-band observations, with the NIRCam filter used for the observation indicated in the title of the panel. The middle panels are the fixed n = 1 Sérsic models of the selected object from GALFIT. The right panels are the residual emission once the modelled galaxy is removed from the observed image. Each panel is a  $3 \times 3 \operatorname{arcsec}^2$  ( $\approx 17 \times 17 \operatorname{kpc}^2$ ) cutout centred on the detected galaxy.



**Figure 2.** The ratio of median extracted  $r_{e, \text{F444W}}$  to model values of mock galaxies (left axis) as a function of model F444W magnitude. For each magnitude, recovered  $r_{e, \text{median}}$  are determined for mock galaxies with model radii of  $\approx 0.4\,\text{kpc}$  (blue dots),  $\approx 0.8\,\text{kpc}$  (orange squares),  $\approx 1.1\,\text{kpc}$  (green triangles),  $\approx 1.4\,\text{kpc}$  (red diamonds), and  $\approx 1.8\,\text{kpc}$  (purple pluses) at z=6.1. The grey dashed line represents  $r_{e, \text{median}}/r_{e, \text{expected}}=1$ , with the grey dotted lines representing  $\pm 0.2$ . We represent the F444W magnitude range our actual sample of HAEs with a grey histogram (right axis). The vertical black lines are the upper and lower bounds of the F444W magnitude range of our HAEs, with the shaded brown regions indicating regions outside of that range.

points represent different  $r_{e, \text{model}}$  values ranging from  $\approx 0.4$  to  $\approx 1.8$  kpc. Overlaid is a histogram of the F444W magnitude counts (right axis) of our sample of 23 HAEs, with vertical black lines indicating the upper and lower bounds of our sample. The shaded regions highlight magnitudes outside the range of our sample. From Fig. 2, we see that for n=1 galaxies at F444W magnitudes

 $\lesssim 26.5$  mag, the recovered  $r_{e,\text{median}}$  are consistent with  $r_{e,\text{model}}$  within uncertainties regardless of  $r_{e,\text{model}}$ . However, at fainter magnitudes, particularly at  $\gtrsim 28$  mag, GALFIT consistently overestimates the sizes, reaching as high as  $\sim$  74 per cent larger for  $r_{e,\text{model}} \approx 0.8 \text{ kpc}$  at 29 mag. This extreme is beyond the range of our sample, however, and all of the ratios for any  $r_{e,\text{model}}$  within our magnitude range are  $\leq 20$  per cent overestimation. This further justifies our floor uncertainty value of 25 per cent for our HAEs in Section 3.1 as a conservative estimate. The general trend from Fig. 2 is that the fainter the magnitude, the more GALFIT overestimates the sizes of known models. We believe this is a result of the sky background becoming more indistinguishable from the faint edges of these objects causing GALFIT to calculate the  $r_e$  of an object that extends further into the sky background than it does in the injected model. This overestimation may introduce some scatter of galaxy sizes at faint magnitudes (see Section 5.1).

# 4 RESULTS

In this section, we detail the key results from our analysis. We do this first by determining whether we observe a  $r_e-M_*$  relationship at z=6.1 and then comparing NB and F444W sizes. The latter allows us to compare the size of the H $\alpha$ -selected SF component of our HAEs to the spatial extent of the established stellar component, inferred from the F444W photometry. Additionally, since both NB filters overlap with F444W, we also fit light profiles to our HAEs with the modelled NB emission removed from the F444W image in order to account for H $\alpha$  contributions to the BB (see Section 4.2.1). In Section 4.3, we will compare our measured  $r_{e, {\rm F444W}}$  to studies at a range of redshifts.

1418

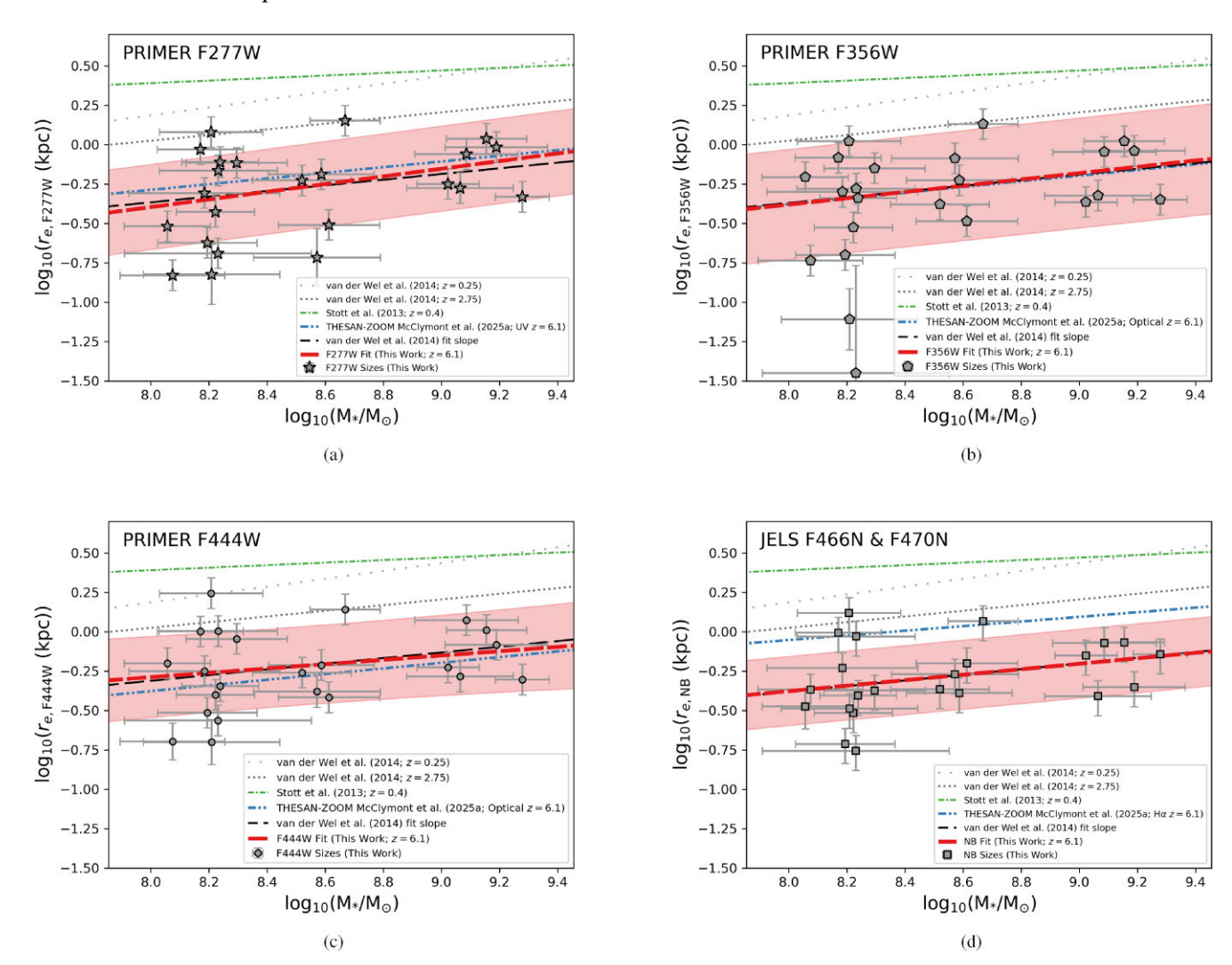


Figure 3. The  $r_e-M_*$  relationship for our HAEs at z=6.1 in four different JWST bands: PRIMER F277W (rest-NUV; upper left), PRIMER F356W (rest-V-band; upper right) and PRIMER F444W (rest-R-band; lower left), and JELS F466N/F470N NB (rest-Hα; lower right). The grey symbols represent the individual sizes of each HAE. In all panels, the red dashed line shows the fitted relationship to the individual points, with the red shaded region indicating the 1σ scatter. We compare to the observed  $r_e-M_*$  relationship of HAEs from J. P. Stott et al. (2013a) at z=0.4 (green dash-dotted line), as well as those from A. van der Wel et al. (2014) at z=0.25 (loosely dotted grey line) and z=2.75 (densely dotted grey line). We also compare to the simulated  $r_e-M_*$  relationship from W. McClymont et al. (2025b) (blue dash-dotted) who employ the THESAN-ZOOM radiation-hydrodynamics zoom-in simulations (R. Kannan et al. 2025). W. McClymont et al. (2025b) measure the  $r_e-M_*$  in three different bands: UV (rest-frame 0.1475 – 1525 μm), optical (rest-frame 0.5 – 0.6 μm), and Hα. We select the appropriate relationship for comparison in each of our observed bands. The black long-dashed line shows the fixed slope of the A. van der Wel et al. (2014)  $r_e-M_*$  relationship at z=2.75 with the offset fitted to our data points.

# 4.1 Size-mass relationship

Fig. 3 shows the  $r_e-M_*$  relationship for our HAEs in the PRIMER F277W (Fig. 3a), PRIMER F356W (Fig. 3b), PRIMER F444W (Fig. 3c), and JELS F466N/F470N NB (Fig. 3d) images. In each panel, the red dashed line indicates the best-fitting power law of the form  $\log_{10}(r_e/\text{kpc}) = \alpha \log_{10}(M_*/\text{M}_\odot) + A$  to the individual  $r_e$  points, determined using the curve\_fit function from the scipy.optimize module in PYTHON (P. Virtanen et al. 2020). The shaded region indicates the  $1\sigma$  scatter at fixed stellar mass. The parameters for these fits can be found in Table 1. We compare to the z=0.4  $r_e-M_*$  relationship of J. P. Stott et al. (2013a) who analysed the structural properties of a sample of HAEs, though we note that their  $r_e$  measurements are determined from ground-based observations (J. E. Geach et al. 2008; D. Sobral et al. 2013). We also

**Table 1.**  $r_e - M_*$  relationships as seen in Fig. 3. These fits are of the form  $\log_{10}(r_e / \text{kpc}) = \alpha \log_{10}(M_*/M_{\odot}) + A$ .

Image	α	A
F277W	$0.24 \pm 0.13$	$-2.34 \pm 1.11$
F356W	$0.20 \pm 0.12$	$-1.98 \pm 1.07$
F444W	$0.14 \pm 0.12$	$-1.39 \pm 1.06$
NB	$0.17 \pm 0.12$	$-1.77 \pm 1.01$
F444W <sub>sub</sub>	$0.08 \pm 0.12$	$-0.82 \pm 1.04$

compare to A. van der Wel et al. (2014) for SF galaxies at  $z \sim 0.25$  (rest-frame *Y*-band; light-grey dotted line) and  $z \sim 2.75$  (rest-frame *B* band; dark-grey dotted line). Despite being at different rest-

frame wavelengths, the observed  $r_e - M_*$  relationships we compare to in Fig. 3 are also measured at wavelengths redward of the rest-4000 Å break so are less affected by ongoing star formation, thus making them reasonable comparisons. We note that these comparisons only apply to BB sizes but we include them on the NB plot for reference. Additionally, we look at how our  $r_e - M_*$ relationship compares to those in simulations from W. McClymont et al. (2025b). They measure the 2D half-light radii of galaxies in the THESAN-ZOOM radiation-hydrodynamics zoom-in simulations (R. Kannan et al. 2025), a high-resolution successor to the large-volume THESAN simulations (R. Kannan et al. 2022). After accounting biases to better match observations, W. McClymont et al. (2025b) measure the  $r_e - M_*$  relationship in three different bands: UV (restframe  $0.1475-1525 \mu m$ ), optical (rest-frame  $0.5-0.6 \mu m$ ) and H $\alpha$ emission. In Fig. 3, we compare each relation from W. McClymont et al. (2025b) to the appropriate observed filter for our sizes. We will focus on the  $r_e - M_*$  relationship in F444W (rest-frame R band) for the rest of this study as it overlaps with the JELS F466N/F470N NB observations and gives a better reflection of the underlying stellar population than bluer BB or the NB data.

From Fig. 3, we observe a  $r_e - M_*$  relationship for HAEs at z = 6.1 with a slope of  $\alpha_{\rm F444W} = 0.14 \pm 0.12$  in F444W and  $\alpha_{\rm H\alpha} = 0.17 \pm 0.12$  in the NB data. The F444W  $r_e - M_*$  relationship is significantly offset from those in both J. P. Stott et al. (2013a) and A. van der Wel et al. (2014), reflecting the accepted trend in the literature that, for fixed stellar mass, galaxies at higher redshifts have smaller  $r_e$  (e.g. T. Shibuya et al. 2015; L. A. Mowla et al. 2019b; W. Sun et al. 2024; A. van der Wel et al. 2024; see Section 4.3). For a fixed stellar mass of  $10^{9.25}$  M<sub> $\odot$ </sub>, we find an offset in  $\log_{10}(r_e / \text{kpc})$  from the A. van der Wel et al. (2014) z = 2.75 relationship of  $-0.37 \pm 0.10$  $(-0.41 \pm 0.10)$  dex for our F444W (NB) derived relationship. We choose to use a fixed stellar mass of  $10^{9.25}\,\mathrm{M}_\odot$  despite being near the upper end of our sample because comparisons in the literature are difficult at lower stellar masses (see Section 4.3). The offset from A. van der Wel et al. (2014) reflects an increase in average  $r_e$  of  $\approx$  1 kpc from z=6.1 to 2.75, or a factor of  $\sim 2.3-2.5$  increase in just  $\sim 1.4$  Gyr. According to A. van der Wel et al. (2014), from z=2.75 to 0.25, the  $r_e$  of a  $10^{9.25}\,\mathrm{M}_\odot$  SF galaxy increases by a factor of  $\approx 1.8$  in  $\sim 8.2$  Gyr, suggesting significantly more rapid galaxy growth before Cosmic Noon than after. This is also indicated by the near-identical value of the z = 0.4 relationship found by J. P. Stott et al. (2013a) at this stellar mass. Similar offsets and slopes to these observational relationships are seen in all filters in Fig. 3. Indeed, from Table 1, all of our  $r_e - M_*$  relationships are consistent within errors, with weak evidence the slope may get shallower with increasing rest-frame wavelength, a trend that has been seen in the literature (K. V. Nedkova et al. 2024; N. Allen et al. 2025; C. Jia et al. 2024; L. Yang et al. 2025).

We find good agreement between our BB  $r_e-M_*$  relations and the simulated z=6.1 results of W. McClymont et al. (2025b), with all trends occupying the  $1\sigma$  scatter about the relationships. This agreement is particularly strong for our PRIMER F356W measurements, where the mean offset is only  $\approx -0.01$  dex in half-light radius across our stellar mass range. In contrast, our z=6.1 H $\alpha$   $r_e-M_*$  relation disagrees with the W. McClymont et al. (2025b) prediction, with their  $r_e$  values  $\approx 0.3$  dex larger. They interpret their large H $\alpha$  sizes as being due to nebula emission beyond the stellar and UV continuum as extreme Lyman-continuum emission from a central starburst region ionizes gas reservoirs surrounding the galaxy. However, our observations do not support this scenario.

The slope of our F444W  $r_e-M_*$  relationship ( $\alpha_{\rm F444W}=0.14\pm0.12$ ) is consistent with those for late-type galaxies in A. van der

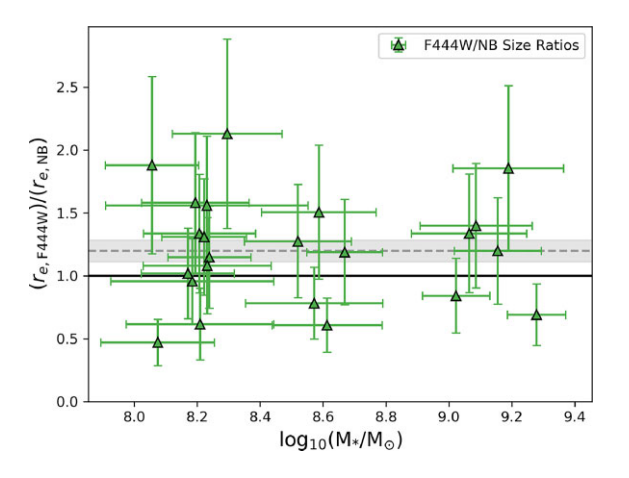


**Figure 4.** The ratio of the measured  $r_e$  in F444W (rest-R band;  $r_{e,\mathrm{F444W}}$ ) to the measured  $r_e$  in NB ( $r_{e,\mathrm{NB}}$ ) for each of our HAEs (green triangles) against stellar mass. The error on each size ratio represents the combined error on the respective  $r_e$  measurements. The solid black line represents  $r_{e,\mathrm{F444W}}/r_{e,\mathrm{NB}} = 1$ . The dashed grey line represents the median  $r_{e,\mathrm{F444W}}/r_{e,\mathrm{NB}} = 1.20$ , with the shaded region indicating the standard error ( $\pm 0.09$ ).

Wel et al. (2014) who find  $\alpha = 0.18 \pm 0.02$  at z = 2.75 and  $\alpha =$  $0.25 \pm 0.02$  at z = 0.25. We illustrate the consistency with A. van der Wel et al. (2014) by fitting a line with a fixed slope equal to their z = 2.75 relationship to our sample (black dashed line) and finding that it is within the  $1\sigma$  scatter of our fit for our full stellar mass range. The large errors on our relationship are likely explained by the much-reduced sample size compared to A. van der Wel et al. (2014; 23 versus  $\sim$  2000) and the large scatter of  $\sigma_{\text{scatter}} = 0.30$  dex of our individual sizes at low stellar mass ( $M_* < 10^{8.4} \, \mathrm{M}_{\odot}$ ; compared to  $\sigma_{\text{scatter}} = 0.16$  dex at  $M_* \ge 10^{8.4} \, \text{M}_{\odot}$ ). We discuss the possible causes of this increased scatter in Section 5.1. We also find that the slope of our  $r_e - M_*$  relationship is consistent within errors with HAE the relationship of J. P. Stott et al. (2013a) at z = 0.4 of  $\alpha =$  $0.03 \pm 0.02$ . These consistencies, although caveated by large relative errors, suggest the trend in the literature that the late-type  $r_e - M_*$ slope remains generally unchanged with redshift may continue out to z = 6.1 (see also L. Shen et al. 2023; K. Ito et al. 2023; E. Ward et al. 2024; N. Allen et al. 2025), though there is evidence of steeper slopes at  $z \lesssim 0.1$  (e.g. S. Shen et al. 2003; Y. Guo et al. 2009; A. Paulino-Afonso et al. 2017). When combined with our H $\alpha$  to stellar continuum size ratios (see Section 4.2), we believe that the lack of significant evolution in the  $r_e - M_*$  slope is a consequence of SF galaxies primarily building their mass through secular star formation across cosmic time. We explore this further in Section 5.2.

# 4.2 Stellar component to star-forming region size ratio

Fig. 4 shows the ratio of  $r_{e, \rm F444W}$  to  $r_e$  measured in NB ( $r_{e, \rm NB}$ ) for each of our HAEs. This ratio reflects the size of any stellar component compared to the SF region traced by H $\alpha$  emission from H II regions surrounding young, massive stars. We find a median size ratio of  $\frac{r_{e, \rm F444W}}{r_{e, \rm NB}} = 1.20 \pm 0.09$ , indicating that the stellar emission is marginally larger than the H $\alpha$ -emitting SF component at the EoR, suggestive of a more centrally concentrated SF regions in HAEs at z=6.1. However, the uncertainty on the measurement of  $\frac{r_{e, \rm F444W}}{r_{e, \rm NB}}$  for many of the individual galaxies is such that the ratio is consistent with 1. Therefore, we can say more broadly that the ratios in Fig. 4 indicate that there are already-established stellar components in SF galaxies at z=6.1 that are at least comparable to, if not larger

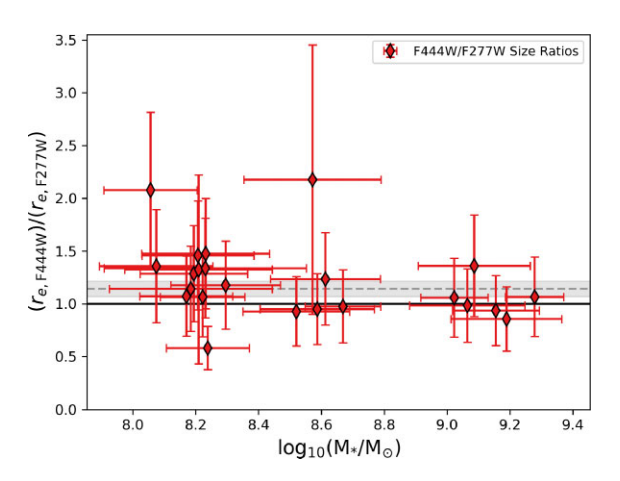


**Figure 5.** As in Fig. 4, but for our  $r_{e,{
m F444W}}$  to  $r_e$  measured in F277W (restNUV;  $r_{e,{
m F277W}}$ ) ratios (thin red diamonds). The dashed grey line and shaded region represent the median  $r_{e,{
m F444W}}/r_{e,{
m F277W}}=1.14\pm0.07$ .

than, the size of the expected SF regions. This contrasts with the results of E. J. Nelson et al. (2016) who find that the active star formation traced by  $H\alpha$  at z=0.7-1.5 extends further than the existing stellar continuum. They conclude that their results show SF galaxies at their redshift range are growing in size primarily from star formation (see also E. J. Nelson et al. 2012; J. Matharu et al. 2022; X. Shen et al. 2024a). D. J. Wilman et al. (2020) see a similar result, finding the median (mean)  $H\alpha$  size being a factor of 1.18 (1.26) larger than the stellar continuum from their sample of 0.7 < z < 2.7 observations using the *K*-band Multi Object Spectrograph (KMOS) in the KMOS<sup>3D</sup> survey (E. Wisnioski et al. 2015, 2019).

As briefly discussed in Introduction, the UV- or NUV-continuum are other frequently used indicators of star formation. Therefore, another method of measuring the extent of any established stellar component to SF regions is to measure the ratio of  $r_{e, \text{F444W}}$  to  $r_e$  measured in F277W (rest-NUV;  $r_{e, \text{F277W}}$ ). We show this in Fig. 5 where we find a median  $\frac{r_{e, \text{F444W}}}{r_{e, \text{F277W}}}$  ratio of  $1.14 \pm 0.07$ . This agrees with our median  $\frac{r_{e, \text{F444W}}}{r_{e, \text{NN}}}$  from Fig. 4 and further suggests that the SF region of our HAEs is more centrally concentrated with an established stellar component that may extend beyond this. This reduced value could also be partly caused by UV light being more affected by dust than H $\alpha$  emission.

Our results imply that, prior to the current period of star formation we are seeing traced by the  $H\alpha$  emission in the NB data, there must have been a significant-enough episode of star formation to form a stellar component with a larger associated  $r_e$ . We discuss the implications and the possible causes of this in Section 5.

#### 4.2.1 Hα contribution to F444W

The nature of NB imaging selection for detecting HAEs mean that there could be a significant contribution from the H $\alpha$  emission line in the overlapping BB emission (in our case contributions to F444W from F466N or F470N). The median observed H $\alpha$  EW for our sample is EW<sub>H $\alpha$ </sub> = 748  $\pm$  89 Å so we decided to run analysis of our HAE sizes where the H $\alpha$  emission is removed from the F444W image to leave an NB flux-subtracted F444W (F444W<sub>sub</sub>) image. To do this, we used the GALFIT output models from the NB fitting and subtracted them from the corresponding F444W image cutouts. This subtraction was done by scaling the NB flux density based on the relative effective widths of the F444W, F466N, and F470N filters.

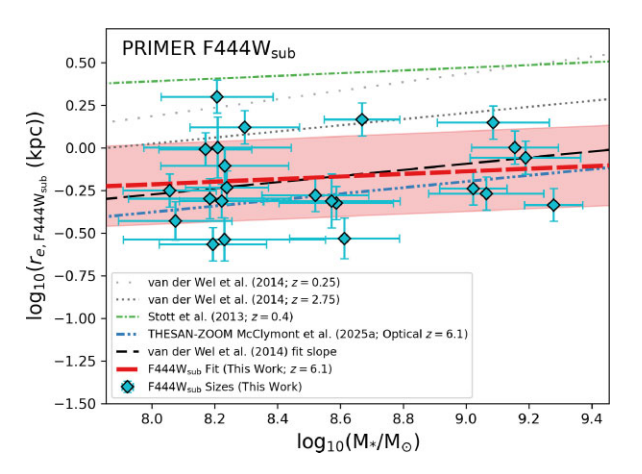


**Figure 6.** The  $r_e-M_*$  relationship as in Fig. 3 for NB flux-subtracted F444W sizes ( $r_{e,F444W_{sub}}$ ; cyan diamonds). The slope here is measured as  $\alpha_{F444W_{sub}}=0.08\pm0.12$  which is shallower than the slope seen measured in Fig. 3(c) driven by an increase in  $r_{e,F444W_{sub}}$  at  $M_*<10^{8.4}\,{\rm M}_{\odot}$ .

The full subtraction is described by

$$f_{\lambda, \text{F444W}_{\text{sub}}} = \frac{f_{\lambda, \text{F444W}} - f_{\lambda, \text{NB}} \left(\frac{W_{\text{eff, NB}}}{W_{\text{eff, F444W}}}\right)}{1 - \frac{W_{\text{eff, NB}}}{W_{\text{eff, F444W}}}},$$
(4)

where  $f_{\lambda}$  and  $W_{\rm eff}$  are the flux density and effective width of a given filter, respectively (W. H. Waller 1990). In our case,  $f_{\lambda, \rm F444W}$  is the flux density of the F444W cutout of our HAEs, and  $f_{\lambda, \rm NB}$  is the flux density of the GALFIT model output in NB, where NB is either F466N or F470N depending on which image the HAE was detected in (see the middle panels of Fig. 1 for example outputs). This method of model subtraction ensures that we are only removing the H $\alpha$  emission from the source without increasing the noise in the sky background, which GALFIT needs for accurate light profiles (C. Y. Peng et al. 2010). Once the NB models have been subtracted from the F444W cutouts, we ran GALFIT on the resulting images following the same steps as Section 3.1.

Fig. 6 shows the  $r_e-M_*$  relationship for our HAEs in the same format as Fig. 3, but using NB flux-subtracted  $r_e$  ( $r_{e,F444W_{sub}}$ ). We find that the slope of this relationship is shallower than those found in Fig. 3 (see Table 1) with  $\alpha_{F444W_{sub}}=0.08\pm0.12$ . However, this is well within  $1\sigma$  of the previous relationships, as well as those from J. P. Stott et al. (2013a) and A. van der Wel et al. (2014).

We measure the ratio of  $r_{e,\text{F444W}_{\text{sub}}}$  to  $r_{e,\text{NB}}$  in Fig. 7. This gives us a cleaner comparison between the size of any stellar components and the SF regions because we have removed contributions from the latter to the BB continuum. We find that the median size ratio when subtracting H\$\alpha\$ emission increases marginally to  $\frac{r_{e,\text{F444W}_{\text{sub}}}}{r_{e,\text{NB}}} = 1.26 \pm 0.14$  (grey dashed line in Fig. 7), compared to  $\frac{r_{e,\text{F444W}}}{r_{e,\text{NB}}} = 1.20 \pm 0.09$  without any subtraction, although the change is not significant. While this is a weak increase within the respective uncertainties, this marginal increase is in line with the SF region traced by H\$\alpha\$ emission being more centrally concentrated.

This average increase in  $r_e$  may contribute to the flattening of our  $r_e-M_*$  slope in Fig. 6 compared to Fig. 3(c), particularly if the increase is predominately in low-mass HAEs. After subtracting H $\alpha$  emission, our  $<10^{8.4}\,\mathrm{M}_\odot$  HAEs have a ratio of  $\frac{r_{e,\mathrm{F444W}_{\mathrm{Sub}}}}{r_{e,\mathrm{F444W}}}=1.10\pm0.32$  compared to  $\frac{r_{e,\mathrm{F444W}_{\mathrm{Sub}}}}{r_{e,\mathrm{F444W}}}=0.98\pm0.04$  for  $\geq10^{8.4}\,\mathrm{M}_\odot$ . The larger errors at  $<10^{8.4}\,\mathrm{M}_\odot$  mean it is difficult to draw any definitive conclusions, and the ratio of both  $r_{e,\mathrm{F444W}}$  and  $r_{e,\mathrm{F444W}_{\mathrm{Sub}}}$  to

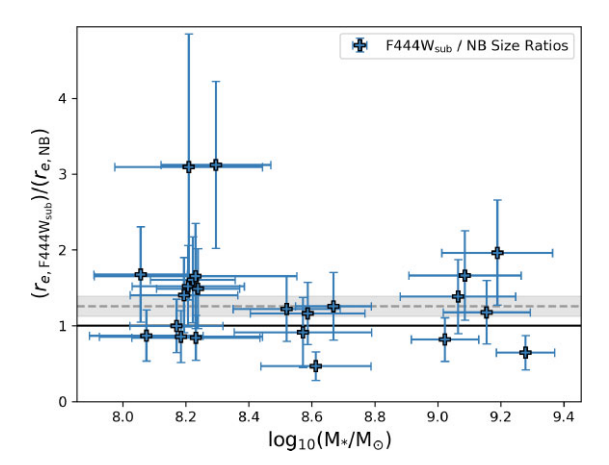


**Figure 7.** As in Fig. 4, but for our NB flux-subtracted F444W  $r_e$  ( $r_{e,F444W_{sub}}$ ) to  $r_{e, NB}$  ratios (blue pluses). The dashed grey line and shaded region represent the median  $r_{e, {
m F444W}_{
m sub}}/r_{e, {
m NB}} = 1.26 \pm 0.14$ , which is marginally larger than than the  $r_{e, \rm F444W}/r_{e, \rm NB} = 1.20 \pm 0.09$  seen in Fig. 4, though consistent within error

 $r_{e,NB}$  are consistent with each other, which suggests the overall sizes are not significantly affected by  $H\alpha$  emission. This is not surprising, since our median observed  $EW_{H\alpha} \sim 750\,\text{Å}$  is  $\approx 7$  per cent the width of the F444W filter ( $W_{\text{eff}} = 10676 \,\text{Å}$ ).

#### 4.3 Redshift evolution of galaxy sizes

The narrow-wavelength range probed by the F466N and F470N filters dictates that the redshift range we can probe for our HAEs is similarly narrow (6  $\lesssim z \lesssim$  6.2, or  $\approx$  0.04 Gyr of cosmic time). As a result, we cannot model the redshift evolution of galaxy sizes across the EoR  $(6 \le z \le 15; X. Fan, C. L. Carilli & B. Keating 2006; B. E. Robertson$ et al. 2013). Instead, we can see how the results from our unbiased, rest-optical HAEs compare to observations in the literature (J. P. Stott et al. 2013a; A. van der Wel et al. 2014, 2024; A. Paulino-Afonso et al. 2017; K. A. Suess et al. 2022; K. Ormerod et al. 2023; M. Martorano et al. 2024; W. Sun et al. 2024; E. Ward et al. 2024; N. Allen et al. 2025), as well as predictions from simulations (X. Wu et al. 2020; W. J. Roper et al. 2022; M. A. Marshall et al. 2022; L. Costantin et al. 2023). These studies measure  $r_e$  of SF galaxies in different ways and we will briefly outline the data of each individual study, all of which are plotted in Fig. 8. We note here that all the observations in the referenced literature measure  $r_e$  in rest-frame optical bands that are redward of the 4000 Å break.

As discussed in Introduction, A. van der Wel et al. (2014) analysed the mass-size relation of galaxies between  $0 \le z \le 3$  from 3D-HST and CANDELS. Here, we look at the size-z relation they find for SF galaxies from their results, as well as individual  $r_e$ values for  $10^{9.25} \,\mathrm{M}_\odot$  SF galaxies at z=0.25 and 2.75 derived from their  $r_e - M_*$  relationships. Note that the derived  $r_e$  values are extrapolations, as A. van der Wel et al. (2014) only fit their late-type galaxy relation for  $\gtrsim 10^{9.48}\,{
m M}_\odot$ . We also compare to the SF  $r_e-M_*$ relation in A. van der Wel et al. (2024), who combine observations from JWST NIRCam in CEERS combined with CANDELS HST imaging. We compare to their median  $r_e$  for  $10^{9.2}\,\mathrm{M}_\odot$  galaxies at z = 1.0 - 1.5 in rest-frame 0.5 µm. K. A. Suess et al. (2022) used data from CEERS and 3D-HST to measure  $r_e$  in the F444W and F150W BB JWST NIRCam filters, with stellar masses measured by R. E. Skelton et al. (2014). For our comparison, we use the rest-frame *R*-band median size of their  $10^{9-9.5}$  M<sub> $\odot$ </sub> SF galaxies at z = 1.3 - 1.7

(median stellar mass  $\approx 10^{9.22} \, \mathrm{M}_{\odot}$ ). We define an SF galaxy from their sample using a U - V < 1.0 colour cut (to distinguish them from passive galaxies) for galaxies that satisfy the R. E. Skelton et al. (2014) 'use' flag = 1, which they define as a galaxy with photometry of reasonably uniform quality. For comparison to K. Ormerod et al. (2023), we used the median size of z = 5 disc-like galaxies derived from their size-z relationship. K. Ormerod et al. (2023) develop their relationship based on CEERS observations in an overlapping region in the CANDELS field, with the median  $r_e$ at z = 5 being measured in F356W of JWST NIRCam (rest-frame R band). N. Allen et al. (2025) measure galaxy sizes from public data from CEERS and PRIMER observations of the COSMOS and UltraDeep survey (UDS) fields accessible via the DAWN JWST Archive (DJA;<sup>5</sup> see F. Valentino et al. 2023). We look at the median  $r_e$  they measure in F444W at the four median redshifts they list in table A.1 of their paper (rest-frame  $0.59 - 1.04 \,\mu\text{m}$ ). From M. Martorano et al. (2024), we compare to both the size-z relation and the derived  $r_e$  of  $\log_{10}(M_{*,\text{median}}/M_{\odot}) \approx 9.27$  SF galaxies from their  $r_e - M_*$  relationship at z = 2 - 2.5. They measured the restframe 1.5  $\mu$ m  $r_e$  for galaxies in COSMOS-WEB (C. M. Casey et al. 2023) and PRIMER-COSMOS. W. Sun et al. (2024) used data from CEERS to measure the  $r_e$  of SF galaxies, fitting 2D parametric models in seven JWST NIRCam filters in both short-wavelength (SW) and LW channels. We compare to the size-z relationship that they derive from their combined rest-frame optical ( $\approx 0.41 - 0.66 \,\mu\text{m}$ ) measurements at z = 4 - 9.5. The final observational result we compare to comes from E. Ward et al. (2024) who also used imaging from CEERS and CANDELS to measure  $r_a$  of galaxies at rest-frame 0.5  $\mu$ m. We extrapolated their  $r_e - M_*$  relation to derive the  $r_e$  of a typical  $10^{9.25} \,\mathrm{M}_{\odot}$  SF galaxy at z = 3 - 5.5.

As with the observations above, we also looked at predictions from various simulations. First, we compared to the rest-frame optical  $r_e$ estimates from the SIMBA cosmological hydrodynamical simulations (R. Davé et al. 2019) as reported by X. Wu et al. (2020). We derived the  $r_e$  of a typical  $10^{9.5} \, \mathrm{M}_{\odot}$  SF galaxy from their size-luminosity relations in SIMBA-25 assuming a D. Calzetti et al. (2000) dust-law and their Sérsic fit method (see their section 3.4). We note that the sizes reported by X. Wu et al. (2020) assume that dust tracks metals and does not assume radiative transfer. We compare to the size-z relation from W. J. Roper et al. (2022) as measured in the First Light And Reionisation Epoch Simulations (FLARES; C. C. Lovell et al. 2020; A. P. Vijayan et al. 2021) – a suite of zoom simulations based on the cosmological hydrodynamical simulations from the Evolution and Assembly of GaLaxies and their Environments (EAGLE: R. A. Crain et al. 2015) project. W. J. Roper et al. (2022) constrain the size z relationship at z = 5 - 10 using rest-UV size measurements. Their size-z relation is based on sizes derived from their non-parametric pixel-based method which they conclude is robust at high-z ( $z \ge 1$ 5; see their section 4.2.2). Despite being primarily based on UV sizes, we note that we find the ratio of  $r_{e,F444W}/r_{e,UV} = 1.14 \pm 0.07$ , suggesting that the V-band emission is slightly larger than the size inferred from the UV continuum, so comparisons to W. J. Roper et al. (2022) should be noted with caution. We also compare to the size-z relationship modelled by L. Costantin et al. (2023) at z = 3 - 6 in the ILLUSTRIS TNG50 cosmological hydrodynamical simulation (P. Torrey et al. 2019; D. Nelson et al. 2019) based on rest-frame optical measurements at  $\approx 0.51 - 0.89 \,\mu\text{m}$ . Finally, we look at the BlueTides cosmological hydrodynamical simulations in M. A. Marshall et al. (2022). The size-z model we use from them

<sup>&</sup>lt;sup>5</sup>https://dawn-cph.github.io/dja/index.html

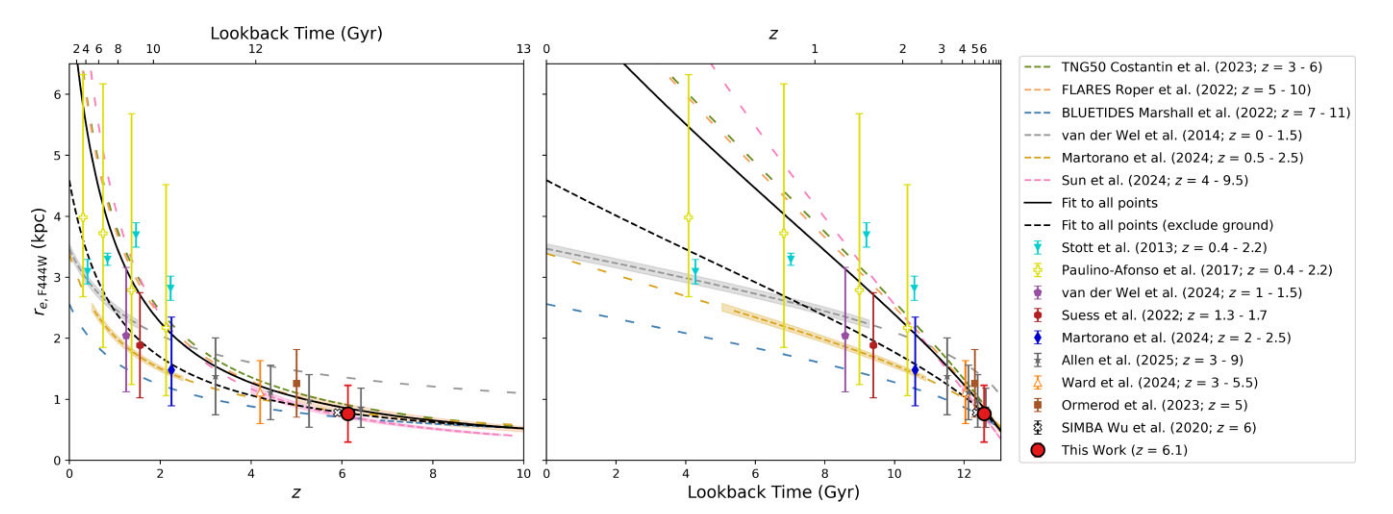


**Figure 8.** Left: size–z relationship of studies in the literature compared to our work. Right: the same as in the left panel, but all points and relations are as a function of lookback time. The large red circle indicates the size of a  $10^{9.25}$  M<sub>☉</sub> SF galaxy for our sample derived from our F444W  $r_e$  −  $M_*$  relationship in Fig. 3(c). The error associated with this size is the scatter about the relationship at this stellar mass. For the individual points, filled faces indicate that the inferred size is derived from a study with a stellar mass (or stellar mass range) that is within the range of this work. White faces indicate that the inferred mass has been extrapolated outside the mass range of that study to match the  $10^{9.25}$  M<sub>☉</sub> we use for our own estimate. We refer the reader to Table 2 for information on these studies. From observations, we compare to the size–z relationships of A. van der Wel et al. (2014) (grey; 0 < z < 1.5), M. Martorano et al. (2024) (yellow; 0.5 < z < 2.5), and W. Sun et al. (2024) (pink; 4 < z < 9.5). From simulations, we compare to the size–z relationship from the TNG50 cosmological hydrodynamical simulation (D. Nelson et al. 2019) in L. Costantin et al. (2023) (green; 3 < z < 6), the FLARES zoom-in simulations (A. P. Vijayan et al. 2021) in W. J. Roper et al. (2022) (orange; 5 < z < 10), and the BlueTides cosmological hydrodynamical simulations (Y. Feng et al. 2016) analysed in M. A. Marshall et al. (2022) (blue; 7 < z < 11). The shaded regions of the literature relationships are the  $1\sigma$  scatter in their relationships within their z range (if applicable). Where the dashed lines become more spaced is an extrapolation beyond the redshift of the respective study. The solid black line is a fit to each of the individual points, weighted by their errors. We also include a fit that does not include the ground-based observations from J. P. Stott et al. (2013a) and A. Paulino-Afonso et al. (2017, dashed black line). The points from A. Paulino-Afonso et al. (

is constrained at z = 7 - 11 based on rest-frame far-UV (FUV), however they find that their FUV and optical sizes are similar so we decided to keep the comparison.

In Fig. 8, we show how the  $r_{e,\mathrm{F444W}}$  of a  $10^{9.25}\,\mathrm{M}_{\odot}$  SF galaxy from our  $r_e-M_*$  relationship (Fig. 3c) compares to the studies mentioned above. We chose to use a stellar mass of  $10^{9.25}\,\mathrm{M}_{\odot}$  for these comparisons rather than our median stellar mass of  $M_{*,\mathrm{median}}=10^{8.30}\,\mathrm{M}_{\odot}$  because the majority of the observational studies derive their size-z evolution models based on much higher characteristic masses. This value is still within our sample's mass range, and is above the mass range where we see the largest scatter in sizes (see Section 5.1). We show the size-z relations as a function of both redshift and lookback time as it is helpful to illustrate to the reader how galaxies grow as a function of linear cosmic time. Details of the studies that compose the individual points in Fig. 8 can be found in Table 2.

From Fig. 8, for a  $10^{9.25}\,\mathrm{M}_{\odot}$  SF galaxy, we predict  $r_{e,\mathrm{F444W}}=0.76\pm0.46\,\mathrm{kpc}$  from our F444W  $r_e-M_*$  relationship (red point). The error associated with this size is the scatter about the relationship at this stellar mass. This  $r_{e,\mathrm{F444W}}$  agrees with a wide range of individual measurements in the literature at z>4 as well as the size-z relationship from W. Sun et al. (2024) at  $z\sim6$ . There is also agreement with the lower z relationship from M. Martorano et al. (2024) extrapolated out to z=6.1. The exception to this is the relationship from A. van der Wel et al. (2014; grey dashed line), constrained between z=0-1.5. Extrapolating their size-z relationship, SF galaxy sizes are  $\approx0.6\,\mathrm{kpc}$  (factor  $\approx1.8$ ) larger at z=6.1 than the other relationships we compare to. On the other hand, the relationship determined from the observations in W. Sun et al. (2024) agrees with our  $r_{e,\mathrm{F444W}}$  at z=6.1, although that relation

overpredicts sizes at much lower redshifts (see also the relations in simulations from W. J. Roper et al. 2022; L. Costantin et al. 2023). The discrepancies between these studies can be explained by the fact their relationships are only measured at certain redshift ranges resulting in them failing to capture galaxy evolution at extrapolated redshifts that are not probed. All the simulated size–z relationships that we compare to agree with our  $r_e$  at z = 6.1.

We fit a power law of the form  $\log_{10}(r_e \ / \ \text{kpc}) = \beta \log_{10}(1+z) + B$  to all the individual points we compare to (solid black line; see Table 2), including our own  $r_{e,\text{F444W}}$ . The parameters of this fit are  $\beta = -1.13 \pm 0.1$  and  $B = 0.89 \pm 0.05$  which predicts  $r_e \approx 7.8$  kpc at z = 0. However, this fit and subsequently inferred  $r_{e,\text{F444W}}$  may be biased by the ground-based observations of HAEs by J. P. Stott et al. (2013a) and A. Paulino-Afonso et al. (2017) from HiZELS, which are less reliable than space-based measurements, and result in a significantly larger size estimate at z = 0. Therefore, we also fit a power law in the same form which excludes these points (dashed black line) with  $\beta = -0.91 \pm 0.09$  and  $B = 0.66 \pm 0.07$ , predicting  $r_e \approx 4.6$  kpc at z = 0.

# 4.4 Merger fraction at z = 6.1

As previously discussed, our final sample of 23 HAEs at z=6.1 is drawn from the parent catalogue of 35 derived by C. A. Pirie et al. (2025). Present in their catalogue of sources – 12 of which we discard from our sample for reasons detailed in Section 2.1 – are some systems with multiple HAEs. Whilst we cannot accurately model the light profiles of those discarded galaxies, we can use them to approximate a merger fraction ( $f_{\rm merger}$ ). This is important to analyse because mergers are one of the primary mechanisms that contribute to

Table 2. The studies that make up the individual points in Fig. 8.

Reference	z	Rest-frame wavelength (µm)	Stellar mass $(\log_{10}(M_*/\mathrm{M}_{\odot}))$
J. P. Stott et al. (2013a)	0.4-2.23	0.47–1.57	9.25
A. Paulino-Afonso et al. (2017)	0.4-2.23	0.25-0.57	9.74-9.96
A. van der Wel et al. (2024)	0.5 - 2.3	0.46-0.57	9.2
K. A. Suess et al. (2022)	1.3-1.7	0.55-0.65	9.22
M. Martorano et al. (2024)	2.0-2.5	1.24-1.45	9.27
N. Allen et al. (2025)	3.0-9.0	0.39-0.62	9.25
E. Ward et al. (2024)	3.0-5.5	0.42-0.58	9.25
K. Ormerod et al. (2023)	5.0	0.48-0.76	9.3-11.1
X. Wu et al. (2020)	6.0	0.62	9.25

galaxy growth (A. Toomre & J. Toomre 1972), including at the EoR (e.g. N. Dalmasso et al. 2024; O. Duan et al. 2025; D. Puskás et al. 2025; L. Westcott et al. 2025; see Section 5.3). To do this, we define a system as a merger if there is another nearby source with a similar photo-z as detected by C. A. Pirie et al. (2025) in their catalogue of PRIMER F356W-detected sources with  $5.5 < z_{\text{phot}} < 6.5$ . We use the parent catalogue of 35 HAEs as the primary galaxies. We also imposed a confidence limit on photo-z for the F356W detections such that the integrated redshift probability distribution function of photo-z fitting, P(z), is limited to detections with P(z) > 0.7. We then counted the number of detections that were within distances of  $d \leq 17$  kpc (corresponding to the width of our GALFIT cutouts),  $d \lesssim 25$  and  $\lesssim 50$  kpc to give a range of estimates for  $f_{\text{merger}}$ . This is a method for determining  $f_{\text{merger}}$  known as 'pair counting' (J. E. Barnes 1988; see also D. R. Patton et al. 1997; O. Le Fevre et al. 2000; E. F. Bell et al. 2006a, b) defined as

$$f_{\text{merger}} = \frac{N_{\text{merger}}}{N_{\text{total}}},\tag{5}$$

where  $N_{\text{merger}}$  is the total number of pairs and  $N_{\text{total}}$  is the total number of galaxies in our primary sample.

We find four systems that have multiple HAEs with  $z_{\rm phot} \sim 6.1$ detected within a 3  $\times$  3 arcsec<sup>2</sup> cutout, equivalent to  $\sim$  17  $\times$  17 kpc<sup>2</sup>. We show these systems in Fig. 9. We smoothed these cutouts with a Gaussian kernel with FWHM (full width half maximum) = 1.5 pixels to reduce some of the noise. We note that in the upper left panel of Fig. 9, galaxy 2266 has a  $z_{\rm phot} = 6.29$  which is within the range required by C. A. Pirie et al. (2025) of  $5.5 < z_{\text{phot}} < 6.5$ , but does not satisfy the other criteria to be in the parent catalogue. Specifically, it has an excess significance parameter in F466N compared to F470N of  $< 2.5\sigma$  and  $< 3\sigma$  compared to F444W which are below the required threshold for a significant detection in F466N compared to either filter. Moreover, while galaxy 2262 has  $> 3\sigma$  excess compared to F444W, its  $z_{\rm phot} = 6.51$  is beyond the range required by C. A. Pirie et al. (2025) to be in the catalogue. We therefore highlight the text for these galaxies in blue to be clear that these are not in the parent catalogue of HAEs. However, given 2266 is a PRIMER F356W detection within the required redshift range, this is considered a merging  $z \approx 6.1$  system with 2282. This potential three-way merger could be an excellent candidate for follow-up with the JWST NIRSpec Integral Field Unit (T. Böker et al. 2022) or the Atacama Large Millimeter Array (A. Wootten & A. R. Thompson 2009).

Pair fractions in the literature are often selected based on the stellar mass ratio,  $\mu$ , of the pair. For *major* mergers, this is typically defined as  $\mu > 1/4$ . Both the JELS parent catalogue of HAEs and the PRIMER F356W-detected catalogue are complete down to  $\approx 10^{8.2}\,\mathrm{M}_{\odot}$ , so to calculate a major merger close-pair

fraction,  $f_{\text{maj. merger}}$ , we set this as a lower mass limit for secondary galaxies, and  $4\times 10^{8.2}\approx 10^{8.8}\,\mathrm{M}_{\odot}$  for primary galaxies. For  $f_{\text{maj. merger}}$ , we also remove any object that exhibits point source activity as the stellar mass values from SED fitting are biased to significantly higher masses. This mass cut, and the removal of point sources, reduces our primary galaxy sample to just nine primary HAEs.

We list our calculated close-pair fractions in Table 3. Within  $d \lesssim 17\,\mathrm{kpc}$ , we find a  $f_\mathrm{merger} = 0.29 \pm 0.09$ , which rises to  $f_\mathrm{merger} = 0.43 \pm 0.11$  ( $f_\mathrm{merger} = 0.71 \pm 0.14$ ) for detections within  $d \lesssim 25\,\mathrm{kpc}$  ( $d \lesssim 50\,\mathrm{kpc}$ ). The systems in Fig. 9 give us a merger fraction  $f_\mathrm{merger} \sim 0.09$  if we only consider NB-detected sources within our cutouts. For  $f_\mathrm{maj.\ merger}$ , our values are consistent with  $f_\mathrm{merger}$ , though we find no examples of major mergers involving multiple HAEs within 17 kpc. We also note that our  $f_\mathrm{maj.\ merger}$  value is dominated by system 2282, which accounts for all pairs within  $d \lesssim 25\,\mathrm{kpc}$ . We compare our merger fractions to values in the literature in Section 5.3.

# 5 DISCUSSION

# 5.1 Scatter of HAE sizes at low stellar mass

From Fig. 3, we see that at low stellar mass  $(M_* < 10^{8.4} \,\mathrm{M}_{\odot})$ , there is a larger scatter in  $\log_{10}(r_e)$  than at high mass for all filters. For example, the scatter of  $\log_{10}(r_{e, \text{F444W}})$  in Fig. 3(c) is  $\sigma_{\text{scatter}} = 0.30$  dex, compared to  $\sigma_{\text{scatter}} = 0.16$  dex at  $M_* \ge 10^{8.4} \,\mathrm{M}_{\odot}$ . This increased scatter at low stellar mass may be a result of the 'bursty' SFH of SF galaxies at the EoR which has been shown to have a greater impact on the evolution of less massive galaxies. Using the Feedback in Realistic Environments (FIRE; P. F. Hopkins et al. 2014) cosmological zoom-in hydrodynamical simulations, K. El-Badry et al. (2016) find that short-term stellar migration ( $\sim 100\,\mathrm{Myr}$ ) can lead to significant fluctuations in  $r_e$  by factors of 2-3 during starbursts, and that this effect is strongest in low-mass galaxies ( $10^{7-9.6} \,\mathrm{M}_{\odot}$ ; see also A. S. Graus et al. 2019; F. J. Mercado et al. 2021). Using the THESAN-ZOOM simulations, W. McClymont et al. (2025a) showed that star formation in the early Universe is highly bursty on short ( $\lesssim 50 \,\mathrm{Myr}$ ) time-scales. Similarly, W. McClymont et al. (2025b) found that the size evolution of SF galaxies is strongly linked to starbursts, with galaxies alternating between phases of compaction and expansion which cause them to 'oscillate' about the  $r_e - M_*$  relationship. This rapid compaction arises because starbursts are typically centrally concentrated, before inside-out quenching subsequently increases their size once the burst subsides. Together, the results of W. McClymont et al. (2025a, b) suggest that EoR galaxies undergo dramatic, short-term morphological transformations driven by bursty

1424

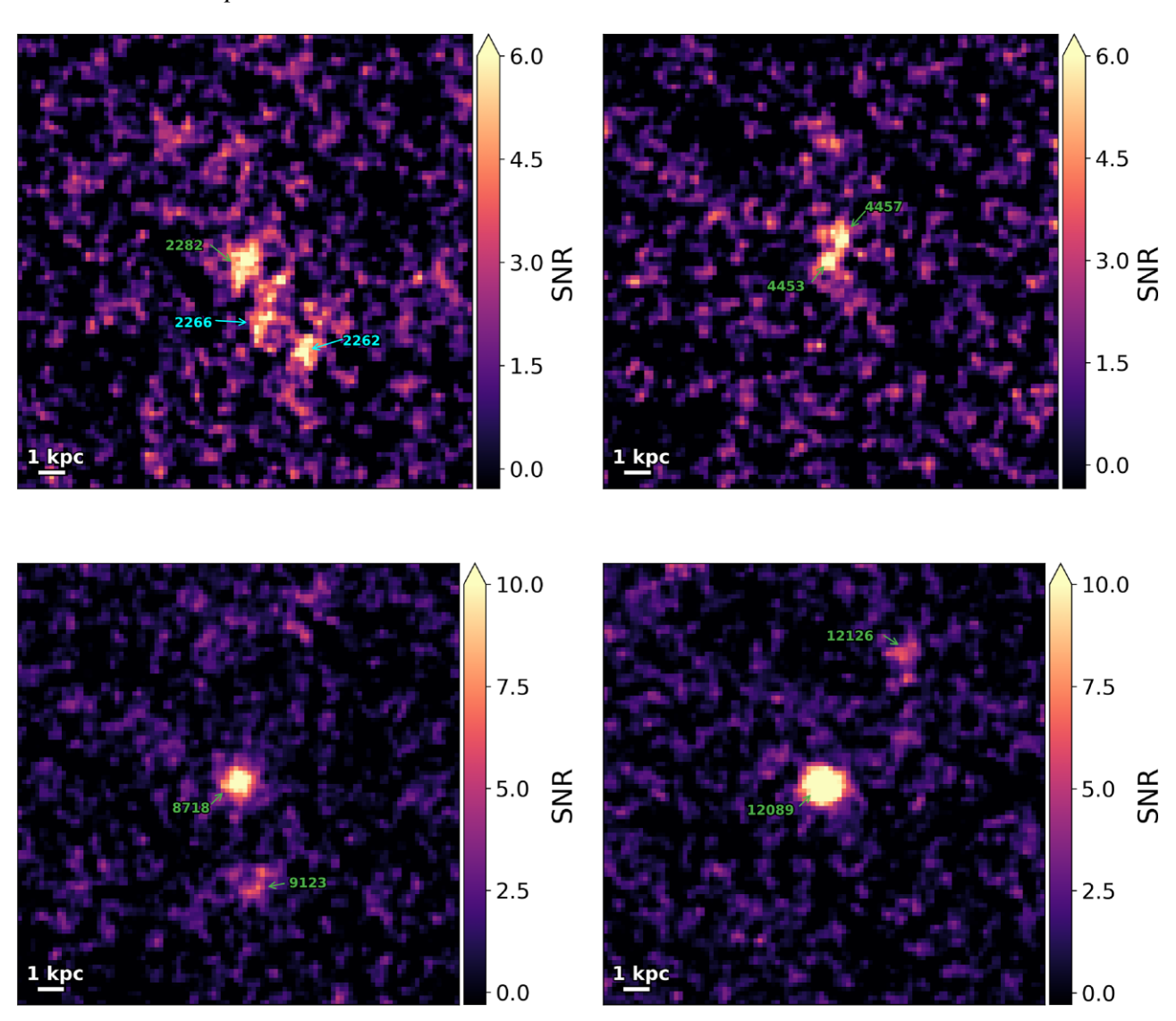


Figure 9.  $3 \times 3$  arcsec<sup>2</sup> ( $\sim 17 \times 17$  kpc<sup>2</sup>) cutouts of four merging systems in JELS F466N smoothed with a Gaussian kernel with FWHM = 1.5 pixels. The colour bar indicates the signal-to-noise ratio per pixel. These cutouts are centred on four different HAE galaxies at z=6.1 and are defined as a merging system from having at least one other NB-selected source within the cutout. Galaxies labelled in green are in the parent catalogue of HAEs from C. A. Pirie et al. (2025). The cutout centred on galaxy 2282 (detected in F466N) has two other candidate sources within the cutout; galaxy 2266 has a similar photo-z to galaxy 2282 ( $z_{\text{phot}} = 6.29$ ), but it has an excess significance parameter in F466N compared to F470N of  $< 2.5\sigma$  and  $< 3\sigma$  compared to F444W which are below the required threshold for a significant detection in F466N compared to either filter; galaxy 2262 has  $> 3\sigma$  excess compared to F444W, but its  $z_{\text{phot}} = 6.51$  is beyond the range required by C. A. Pirie et al. (2025) to be in the catalogue of 5.5  $< z_{\text{phot}} < 6.5$ . These galaxies are therefore highlighted in blue to be clear that these are not in the parent catalogue of HAEs.

**Table 3.**  $f_{\text{merger}}$  from equation (5) for PRIMER F356W-detected sources within fixed distances, d, from systems in the parent catalogue of HAEs in C. A. Pirie et al. (2025).

d (kpc)	$f_{ m merger}$	$f_{ m maj.\ merger}$	
17 (HAEs only) <sup>a</sup>	$0.09 \pm 0.05$		
17	$0.29 \pm 0.09$	$0.33 \pm 0.19$	
25	$0.43 \pm 0.11$	$0.44 \pm 0.22$	
50	$0.71 \pm 0.14$	$0.67 \pm 0.27$	

Note. <sup>a</sup>Only considering other HAEs within the GALFIT cutouts.

SFHs, potentially contributing to the scatter we observe in our  $r_e - M_*$  relations. The SFH of our HAEs, determined from SED fitting by C. A. Pirie et al. (2025), is explored in greater detail in Section 5.2.

Given the assumption that the large scatter at low stellar masses may be caused by diverse SFH, as well as evidence in the literature from simulations, we looked for a connection between  $r_{e,\mathrm{F444W}}$  and the SF properties of these  $\lesssim 10^{8.4}\,\mathrm{M}_\odot$  HAEs. We did not find any correlation between  $r_{e,\mathrm{F444W}}$  and current SFR measured from H $\alpha$ , UV continuum or SFR derived from SED fitting. Only a weak correlation is found between  $r_{e,\mathrm{F444W}}$  and the ratio of SED-fitted SFR averaged over canonical time-scales of 10 Myr to SFR averaged over 100 Myr (SFR<sub>10</sub>/SFR<sub>100</sub>), with a relationship in the form SFR<sub>10</sub>/SFR<sub>100</sub> = (0.58  $\pm$  0.65) $r_{e,\mathrm{F444W}}$  + (3.24  $\pm$  0.51), though we note the sample size for this fit is only 12 HAEs. SFR<sub>10</sub>/SFR<sub>100</sub> is a proxy of the burstiness of star formation (e.g. A. Broussard et al. 2019) and, as such, gives a good indication of the recent SFH of these galaxies, with C. A. Pirie et al. (2025) showing that the HAEs in the parent catalogue, particularly those at low stellar mass, are undergoing a

recent upturn in star formation (see Section 5.2 for further details). However, this analysis is only able to get an estimate of the time averaged SFR over  $\leq 100\,\mathrm{Myr}$ , which is the SFH from  $z \approx 6.7$ . It is entirely possible that these galaxies may have undergone previous starbursts at  $z \gtrsim 6.7$  (see Section 4.2) which have contributed to the scatter we observe in the  $r_e-M_*$  relationship at z=6.1.

Our analysis in Section 3.1.1 shows that mock galaxies with magnitudes  $\gtrsim 27.5$  mag and  $r_e \lesssim 0.8$  kpc have overestimated  $r_{e, \text{median}}$  recovered by GALFIT compared to  $r_{e, \text{model}}$  (see Fig. 2). While  $r_{e, \text{median}}/r_{e, \text{model}}$  does not exceed a factor of 1.2 within the magnitude range of our sample, it is plausible that some of the less massive HAEs (which tend to be fainter) are contributing to this scatter because they have elevated  $r_e$  compared to their real size.

Additionally, as explored in Section 4.2.1, we found some evidence that the F444W sizes of HAEs at  $< 10^{8.4} \, \rm M_{\odot}$  are more impacted by the removal of H\$\alpha\$ contribution to the overlapping F444W, with  $r_{e, \rm F444W_{sub}}$  being larger than  $r_{e, \rm F444W}$  by factor of  $1.10 \pm 0.32$  (Fig. 7). We also find that the scatter in  $\log_{10}(r_{e, \rm F444W_{sub}})$  reduces to  $\sigma_{\rm scatter} = 0.25$  dex. This suggests that the scatter in F444W at low stellar mass is being contributed to by H\$\alpha\$ emission in the BB, though this does not explain the scatter observed in other filters which are also  $\gtrsim 0.3$  dex. Ultimately, it is likely that a combination of all the reasons discussed above are contributing to the scatter of HAE sizes.

# 5.2 Implications for inside-out growth of galaxies

From Fig. 4, we find that the physical sizes of the stellar continuum of z = 6.1 SF galaxies are marginally bigger than sizes inferred from their  $H\alpha$  emission. Given that the ratio for many of the individual objects is consistent with  $\frac{r_{e, \text{F444W}}}{r_{e, \text{NB}}} = 1$ , we can say that, at the very least, our results show that a significant stellar population has been built-up by the end of the EoR that is comparable to the size of the SF component and that this SF region may be more centrally concentrated. It should be noted that using the H $\alpha$  emission as a direct proxy for the extent of the SF component of galaxies can have its complications as a result of potential dust obscuration of the rest-frame optical light (e.g. S. Wuyts et al. 2011; E. J. Nelson et al. 2012; S. Tacchella et al. 2015). However, from their BAGPIPES<sup>6</sup> (A. C. Carnall et al. 2018) SED fitting, C. A. Pirie et al. (2025) have demonstrated that our sample of HAEs are relatively dust-poor with a median  $A_V = 0.23$ . Indeed, rest-frame R-band light is less susceptible to dust attenuation compared to rest-UV emission (D. Calzetti et al. 2000; S. Salim et al. 2018), which is often used in the literature to identify SF regions (e.g. E. J. Murphy et al. 2011; M. Mosleh et al. 2012; Y. Ono et al. 2023; T. Morishita et al. 2024) so any impacts on our overall sizes will not be as great as those studies. Additionally, we are observing the ratio of the stellar component to the SF region at approximately the same wavelength between the NB and F444W filters ( $\lambda \approx 4.4 - 4.7 \,\mu \text{m}$  rest-frame R band). Therefore, should there be any significant impact from dust, it would affect the sizes in both the NB and F444W images approximately the same. A caveat to this is the possibility there may be a difference in the dust extinction for the stellar continuum and nebular components, but this remains uncertain at high-z (R. L. Sanders et al. 2025).

Evidence in the literature suggests that galaxies experience what is known as 'inside-out' growth (P. G. van Dokkum et al. 2010). In this paradigm, galaxies predominantly grow their mass and sizes from centrally concentrated SF regions first before expanding out into, and indeed forming, an extended stellar discs towards lower redshifts.

<sup>6</sup>https://bagpipes.readthedocs.io

This transition of primary mass/size build-up from central regions to extended disks has been shown to come from either elevated SFRs in the diskc compared to the central bulge (e.g. A. Dekel & A. Burkert 2014; A. Zolotov et al. 2015; S. L. Ellison et al. 2018; L. Shen et al. 2024b) or from wet mergers (e.g. J. C. Mihos & L. Hernquist 1994; L. Lin et al. 2008; S. Lapiner et al. 2023). Whilst this is a reasonably well-known evolutionary track from Cosmic Noon, when the global SFR peaks ( $1 \le z \le 3$ ; P. Madau & M. Dickinson 2014), only recently has JWST allowed inside-out growth to be observed directly, and in greater detail, out to the EoR. For example, W. M. Baker et al. (2025) discovered a mature SF galaxy at z = 7.43 in the Great Observatories Origins Deep Survey-South (GOODS-S) field (M. Giavalisco et al. 2004) from the JWST Advanced Deep Extragalactic Survey (JADES; D. J. Eisenstein et al. 2023). From this, they were able to ascertain the recent and extended SFH of the galaxy which shows that the time-averaged SFR over the prior 100 Myr was highest in the central core of the galaxy, but over the most recent 10 Myr, the SFR is significantly higher in the disc, consistent with inside-out growth. Other studies have show similar consistencies with inside-out growth at  $z \gtrsim 6$  (e.g. T. Morishita et al. 2024; J. Matharu et al. 2024; D. D. Kocevski et al. 2025). More generally, prior to the launch of JWST, observations found that rest-frame optical emission lines in galaxies at  $z \gtrsim 6$  had high rest-frame EWs ( $\geq 500 \,\text{Å}$ ; e.g. I. Labbé et al. 2013; R. Smit et al. 2015; G. W. Roberts-Borsani et al. 2016; R. Endsley et al. 2020; M. Stefanon et al. 2022), indicating strong specific SFR (sSFR)s at these redshifts which could imply rapid growth that aligns with the inside-out paradigm.

However, whilst evidence exists that galaxies evolve inside-out during the EoR, it is becoming apparent that the SFH of galaxies at this epoch are complex and diverse. Galaxies have been shown to go through bursts of star formation (often referred to as bursty SFH; A. Dressler et al. 2023, 2024; L. Ciesla et al. 2024; A. Harshan et al. 2024; B. Wang et al. 2024b; T. J. Looser et al. 2025), which were previously predicted by simulations prior to JWST (T. Kimm & R. Cen 2014; D. Ceverino, R. S. Klessen & S. C. O. Glover 2018; S. R. Furlanetto & J. Mirocha 2022). Recently, R. Endsley et al. (2025) analysed 368  $z \sim 6$  Lyman-break galaxies in the GOODS fields and lensed fields surrounding the A2744 cluster and found a dramatic range of SFHs. They analyse the H $\alpha$  to UV luminosity ratio  $(L_{\rm H\alpha}/L_{\rm UV})$  to infer the recent SFH of their galaxies and find their sample has properties consistent with extremely bursty SFHs, as well as finding that many of their galaxies have experienced strong recent SFR upturns and downturns. This followed a similar result from R. Endsley et al. (2024) who similarly concluded that  $z \gtrsim 6$  galaxies experienced bursty SFHs with evidence of strong recent downturns, this time using [O III],  $H\beta$ , and  $H\alpha$  EWs.

For our sample of HAEs, C. A. Pirie et al. (2025) have demonstrated that they are going through a recent burst of star formation from their SED fitting, particularly those with stellar masses  $M_* \lesssim 10^9 \, \mathrm{M}_\odot$ . As they point out, this was to be expected as  $\mathrm{H}\alpha$  emission is a good tracer of recent star formation ( $\approx 10 \, \mathrm{Myr}$ ; E. J. Murphy et al. 2011) compared to the UV-continuum, for example, which can be used to probe longer time-scales ( $\gtrsim 100 \, \mathrm{Myr}$ ; J. Hao et al. 2011a), though we caveat that UV emission is produced by a combination of different stellar populations that range in lifespans ( $\sim 10 - 200 \, \mathrm{Myr}$ ), meaning it can only be confidently used to trace stellar populations older than  $\gtrsim 100 \, \mathrm{Myr}$  in galaxies with steady-state star formation. However, in line with the studies we mention above, C. A. Pirie et al. (2025) find that their results indicate that these HAEs at z = 6.1 have bursty SFHs.

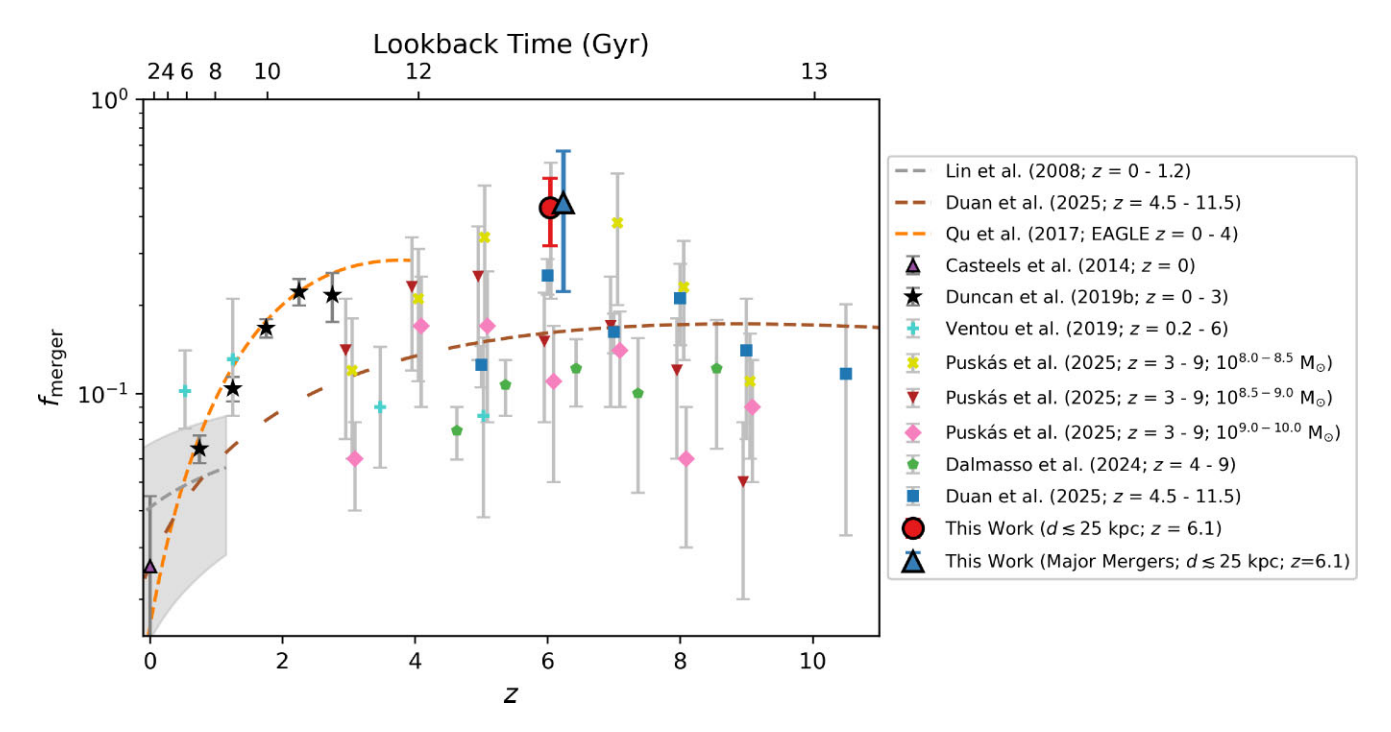


Figure 10. Our measured close-pair merger fraction,  $f_{merger}$ , based on PRIMER F356W detections at  $z_{phot} \sim 6$  within  $d \lesssim 25$  kpc of HAEs in the parent catalogue of C. A. Pirie et al. (2025; large red circle). The large blue triangle represents our pair fraction for major mergers,  $f_{maj. merger}$ , with a stellar mass ratio of  $\mu > 1/4$ . Our  $f_{merger}$  ( $f_{maj. merger}$ ) value is offset by +(-)0.1 in redshift for clarity. The error on all individual points represent the standard error of the measured fraction at that redshift. Most comparisons in the literature use a similar close-pair fraction method to the one in this study, with the exception of N. Dalmasso et al. (2024) who use morphological statistical parameters for their fraction. The dashed lines from Y. Qu et al. (2017) and Q. Duan et al. (2025) show the redshift evolution of merger fractions as a power law with an additional exponential component of the form  $f_{merger} = f_0 \cdot (1 + z)^m \cdot e^{\tau(a+z)}$ . The grey dashed line indicates the power-law evolution measured by L. Lin et al. (2008) at z = 0 - 1.2 based on analysis of close-pair fractions. Their relationship is of the form  $f_{merger} = f_0 \cdot (1 + z)^m$ , with the grey shaded region indicating the  $1\sigma$  error of their relationship. The brown dashed line is the observed evolution measured by Q. Duan et al. (2025) between z = 4.5 - 11.5, who use K. R. V. Casteels et al. (2014) as their z = 0 point. Where the Q. Duan et al. (2025) relationship becomes more spaced is where we extrapolate beyond their redshift range. The orange dashed line indicates the redshift evolution from the EAGLE cosmological hydrodynamical simulations (R. A. Crain et al. 2015) as measured by Y. Qu et al. (2017) from z = 0 - 4.

In this context, given our results in this paper show that a significant stellar component has already been built up, and that the results of C. A. Pirie et al. (2025) show that these same galaxies are currently undergoing a burst of star formation (especially those at  $M_* \lesssim 10^9 \,\mathrm{M}_{\odot}$ ), we conclude that the stellar component must have been built by some previous episodes of star formation and that these were likely bursts themselves. Moreover, we also believe that these episodes of star formation may have occurred at  $z \gtrsim 6.7$ ( $\approx 100 \, \text{Myr}$  prior to z = 6.1) since the median SFR<sub>10</sub>/SFR<sub>100</sub>  $\approx 2.9$ for our sample of 23 HAEs, suggesting the recent burst is significantly elevated compared to the averaged 100 Myr SFR. These bursts of star formation may then be regulated by stellar feedback (i.e. X. Ma et al. 2018; H. Katz et al. 2023; X. Shen et al. 2024a) and/or mergers (see Section 5.3). This is not necessarily in contradiction to inside-out growth evolution, as C. A. Pirie et al. (2025) have shown that higher mass sources  $(M_* \gtrsim 10^9 \,\mathrm{M}_{\odot})$  show evidence of a more consistent SFH. Additionally, the stochastic SFH exhibited by these sources may consistently be centrally concentrated given we are observing the current SF region as being marginally smaller than the stellar component on average. This is best illustrated when we compare  $r_{e,F444W_{sub}}$  to  $r_{e,NB}$  and find that NB flux-subtracted F444W sizes are a factor of  $1.26 \pm 0.14$  larger, which suggests a centrally concentrated SF region. Stars formed during these bursts may then 'fan' out with time as a result of stellar migration (R. Schönrich & J. Binney 2009; K. El-Badry et al. 2016) in a manner consistent with

inside—out growth. Given the evidence of bursty star formation in the literature combined with our results, we suggest that a more complex approach to galaxy evolution is needed at the EoR.

# 5.3 Merger fraction comparisons

In this section, we will compare our measured  $f_{\rm merger}$  and  $f_{\rm maj.\ merger}$  to values in the literature, from both observations and simulations. For the purposes of all comparisons, we will use our estimates at  $5.5 < z_{\rm phot} < 6.5$  within  $d \lesssim 25$  kpc (see Table 3) as this is the most comparable value to the comparison studies in Fig. 10.

Fig. 10 shows how our close-pair fractions at z=6.1 compare to measurements in the literature for a range of redshifts. Most of these measurements use a similar close-pair fraction methodology to this work, with the exception of N. Dalmasso et al. (2024, green pentagons) who use a combination of morphological statistical parameters, and we refer the reader to their paper for details on their methods. We highlight here that direct comparisons to their work should be noted with caution due to potential systematic effects that arise from the differences between our methods. We also note that the z=0  $f_{\rm merger}$  from K. R. V. Casteels et al. (2014, purple triangle) is used by Q. Duan et al. (2025) as a supplementary zero-point for their  $f_{\rm merger}$ –z relationship (brown dashed line). All of the merger fractions at  $z\gtrsim 3$  in Fig. 10, as well as the K. R. V. Casteels et al. (2014) value, are based on galaxy samples with a comparable stellar mass range to

our own. The merger fractions of K. Duncan et al. (2019, black stars; typical stellar mass  $M_* \sim 10^{10}\,{\rm M}_\odot$ ), and the relation from L. Lin et al. (2008, grey dashed line and shaded region;  $M_* \sim 10^{10.7}\,{\rm M}_\odot$ ) are based on stellar mass ranges that exceed our sample.

From Fig. 10, we can see that our measured close-pair fractions of  $f_{\rm merger}=0.43\pm0.11$  and  $f_{\rm maj,\ merger}=0.44\pm0.22$  broadly agree with literature values at z=6.1 within uncertainty, though we find they are higher than the relationship of Q. Duan et al. (2025) and the values from N. Dalmasso et al. (2024). We particularly find excellent agreement with the  $f_{\rm merger}$  from D. Puskás et al. (2025). Their results are derived from JADES observations of the GOODS-North (GOODS-N) and GOODS-S fields at  $z\sim3-9$  for separations of 5< d<30 kpc. As a result of their large sample size ( $\sim300\,000$ ), they split their  $f_{\rm merger}$  into different stellar mass ranges, and we find the best agreement with their  $10^{8.0-8.5}\,{\rm M}_{\odot}$  values. This range also best matches the stellar mass of the parent catalogue of JELS HAEs ( $M_{*,\rm median}=10^{8.36}\,{\rm M}_{\odot}$ ). Specifically, in this mass range, they find  $f_{\rm merger}=0.41\pm0.20$  at 5.5< z<6.5 which is consistent with all of our  $f_{\rm merger}$  and  $f_{\rm maj,\ merger}$  values in Table 3.

Compared to the z = 0  $f_{\text{merger}}$  from K. R. V. Casteels et al. (2014), we find that close-pair fractions at z = 6.1 are a factor of  $\sim 12$ higher than the local Universe for  $d \lesssim 25$  kpc. Comparing instead to the z = 0 value inferred from the L. Lin et al. (2008) relationship, our close-pair fractions is a factor of  $\approx 8$  higher. Both of these comparisons demonstrate that the merger rate of galaxies during the EoR is significantly higher than the local Universe, as also indicated by the other studies in Fig. 10. However, there is evidence in the literature that the galaxy merger rates rise from z = 0 before flattening and remaining consistent at  $z \ge 3$ , which is seen in both the observed  $f_{\text{merger}}$ -z relationship in Q. Duan et al. (2025) and results from the EAGLE simulations in Y. Qu et al. (2017, see Fig. 10; see also C. J. Conselice 2014; C. J. Mundy et al. 2017; J. A. O'Leary et al. 2021; F. Huško, C. G. Lacey & C. M. Baugh 2022; L. Westcott et al. 2025). Our results in Table 3 for all separations, combined with results in the literature, suggest that galaxy mergers play an important role in galaxy evolution at the EoR.

# 6 CONCLUSIONS

We utilized data from the JELS (GO no. 2321; PI: Philip Best; see K. J. Duncan et al. 2025; C. A. Pirie et al. 2025) to study the sizes of 23 HAEs at z = 6.1. Our sample is drawn from a parent catalogue of 35 HAEs described in C. A. Pirie et al. (2025). We measured the size of both the ionize H $\alpha$  emission from  $\lambda \sim 4.7 \,\mu m$  NB data taken by JELS, and the stellar emission from  $\lambda \sim 4.4 \,\mu m$  PRIMER F444W images (both rest-R-band). In addition, sizes were also measured in PRIMER F277W (rest-NUV) and PRIMER F356W (rest-V-band) to allow us to compare the light profiles of different stellar populations at the EoR. We determine the sizes of galaxies from their half-light radii  $(r_e)$  which is measured using n = 1 Sérsic light profiles from GALFIT. We used these values to determine the size–mass  $(r_e - M_*)$ relationship of SF galaxies at this epoch and compare to studies at lower redshift. We compared the average  $r_{e,F444W}$  of our sample to a range of observational and simulated results in the literature from z = 0 - 11. Using robust photo-z detections in F356W at z = 6.1, we were also able to determine an estimate of the merger fraction  $(f_{\text{merger}})$  of galaxies during the EoR. Our key results are summarized as follows:

(i) We observe a  $r_e-M_*$  relationship in our sample of HAEs in all observed NIRCam filters (Fig. 3 and Table 1). Our  $r_e-M_*$  relationships are offset from those found at lower redshift. We find

an offset of  $-0.37 \pm 0.10$  dex in  $\log_{10}(r_{e, \text{F444W}} / \text{kpc})$  to the A. van der Wel et al. (2014) relationship at z = 2.75 for a fixed stellar mass of  $10^{9.25} \, \text{M}_{\odot}$ . This offset reflects a  $\sim 2.3 - 2.5$  factor increase in the sizes of the stellar component between z = 6.1 and  $2.75 \, (\approx 1.4 \, \text{Gyr})$ , suggesting SF galaxies grow rapidly from the EoR to Cosmic Noon.

- (ii) We measure the slope of the F444W $r_e-M_*$  relationship to be  $\alpha_{\rm F444W}=0.14\pm0.12$  (Fig. 3c). This slope is consistent with those found by A. van der Wel et al. (2014) at both z=0.25 and z=2.75 as well as the  $r_e-M_*$  slope of HAEs at z=0.4 found by J. P. Stott et al. (2013a). These results suggest that there is no significant redshift evolution in the slope of the  $r_e-M_*$  relationship between  $0.3 \lesssim z \lesssim 6.1$ .
- (iii) The average  $r_{e, \rm F444W}$  of a  $10^{9.25}\,{\rm M}_{\odot}$  SF galaxy at z=6.1, inferred from our  $r_e-M_*$  relationship, is  $0.76\pm0.46\,{\rm kpc}$ . This value is in excellent agreement with a wide range of literature values at z=6.1, both from observations and simulations (Fig. 8).
- (iv) We measured the ratio of the F444W sizes to NB sizes for each of the galaxies in our sample (Fig. 4). This traces the size ratio of any established stellar component to the SF region traced by ionized gas. We find that the median ratio of these sizes is  $\frac{r_{e, \text{F444W}}}{r_{e, \text{NB}}} = 1.20 \pm 0.09$ . Using rest-NUV as a tracer of active star formation, we find  $\frac{r_{e, \text{F277W}}}{r_{e, \text{F277W}}} = 1.14 \pm 0.07$  (Fig. 5). These measured ratios imply that SF galaxies at z = 6.1 have an already-established stellar component that is at least comparable to the size of the SF region just  $\sim 900$  Myr after the big bang. This also agrees with SF galaxies exhibiting more centrally concentrated star formation at the EoR.
- (v) Previous analysis from C. A. Pirie et al. (2025) indicates that these galaxies are undergoing a strong, recent starburst, with our sample of 23 HAEs showing a median SFR<sub>10</sub>/SFR<sub>100</sub>  $\approx 2.9$ . Given the evidence in the literature that galaxies at the EoR have bursty SFH, we suggest that the established stellar component we observe in our sample may have resulted from episodes of star formation at  $z\gtrsim 6.7$  ( $\gtrsim 100\,\mathrm{Myr}$  prior to z=6.1). Additionally, we believe the large scatter ( $\sigma_{\mathrm{scatter}}\sim 0.30$ ) in the  $r_e-M_*$  relationship at  $M_*<10^{8.4}\,\mathrm{M}_\odot$  is being significantly contributed to by low-mass galaxies being more affected by bursts of star formation giving them more diverse SFH. This could also be affected by GALFIT overestimating  $r_e$  at faint magnitudes (Fig. 2).
- (vi) We determine a close-pair fraction using close-pair counting based on PRIMER F356W  $z_{\rm phot}\sim 6$  detections from C. A. Pirie et al. (2025) and their parent HAE catalogue. We find  $f_{\rm merger}=0.43\pm0.11$  at z=6.1 using a galaxy separation of  $d\lesssim 25\,{\rm kpc}$ . Using a stellar mass ratio of  $\mu<1/4$ , we determine a close-pair fraction for major mergers of  $f_{\rm maj.\ merger}=0.44\pm0.22$ . These values agree with merger fractions in the literature at the EoR (Fig. 10). This shows mergers play an important role in galaxy growth from the EoR to Cosmic Noon.

# **ACKNOWLEDGEMENTS**

This work makes use of ASTROPY, <sup>7</sup> a community-developed core PYTHON package for Astronomy (Astropy Collaboration 2013, 2018, 2022), as well as the NUMPY (C. R. Harris et al. 2020) and SCIPY (P. Virtanen et al. 2020) packages (see also T. E. Oliphant 2007). All plots were created using the MATPLOTLIB 2D graphics PYTHON package (J. D. Hunter 2007). Conversions between redshift and lookback time in our selected cosmological model were done using the Javascript cosmological calculator from E. L. Wright (2006). <sup>8</sup>

<sup>&</sup>lt;sup>7</sup>http://www.astropy.org

<sup>8</sup>https://astro.ucla.edu/~wright/CosmoCalc.html

# 1428 H. M. O. Stephenson et al.

The authors would like to thank the anonymous referee for their constructive comments and suggestions which have strengthened the analysis of this work and improved the paper. The authors also gratefully acknowledge Ian Smail for providing valuable feedback and helping to guide the science of this paper. This work is based on observations made with the NASA/ESA/CSA James Webb Space Telescope. The data were obtained from the Mikulski Archive for Space Telescopes at the Space Telescope Science Institute, which is operated by the Association of Universities for Research in Astronomy, Inc., under NASA contract NAS 5-03127 for JWST. These observations are associated with programs GO no. 2321 (JELS) and GO no. 1837 (PRIMER). The authors acknowledge the PRIMER team for developing their observing program with a zero-exclusive-access period. HMOS acknowledges support from an STFC PhD studentship and the Faculty of Science and Technology at Lancaster University. PNB is grateful for support from the UK STFC via grants ST/V000594/1 and ST/Y000951/1. JSD acknowledges the support of the Royal Society via a Royal Society Research Professorship. LOF acknowledges funding by ANID BECAS/DOCTORADO NACIONAL 21220499. CLH acknowledges support from the Oxford Hintze Centre for Astrophysical Surveys which is funded through generous support from the Hintze family charity foundation. EI gratefully acknowledge financial support from ANID - MILENIO -NCN2024\_112 and ANID FONDECYT Regular 1221846.

For the purpose of open access, the authors have applied a Creative Commons attribution (CC BY) licence to any author-accepted manuscript version arising.

# DATA AVAILABILITY

The original data underlying this article are available from the Mikulski Archive for Space Telescopes at https://doi.org/10.179 09/8v6n-ad45. Higher level data products, including all reduced mosaics in the JELS NB and BB filters (v0.8 and v1.0) presented in K. J. Duncan et al. (2025), as well as associated catalogues described in C. A. Pirie et al. (2025), are made available through the Edinburgh DataShare service. Any other data produced for the article will be shared on reasonable request to the corresponding author.

# REFERENCES

```
Algera H. S. B. et al., 2023, MNRAS, 518, 6142
Allen N. et al., 2025, A&A, 698, A30
Arrabal Haro P. et al., 2023, Nature, 622, 707
Astropy Collaboration, 2013, A&A, 558, A33
Astropy Collaboration, 2018, AJ, 156, 123
Astropy Collaboration, 2022, ApJ, 935, 167
Bagley M. B. et al., 2023, ApJ, 946, L12
Baker W. M. et al., 2025, Nat. Astron., 9, 141
Barnes J. E., 1988, ApJ, 331, 699
Bell E. F. et al., 2006a, ApJ, 640, 241
Bell E. F., Phleps S., Somerville R. S., Wolf C., Borch A., Meisenheimer K.,
   2006b, ApJ, 652, 270
Bertin E., Arnouts S., 1996, A&AS, 117, 393
Böker T. et al., 2022, A&A, 661, A82
Bouwens R. et al., 2020, ApJ, 902, 112
Bouwens R. J. et al., 2012a, ApJ, 752, L5
Bouwens R. J. et al., 2012b, ApJ, 754, 83
Bouwens R. J. et al., 2015, ApJ, 803, 34
```

```
Bowler R. A. A., Cullen F., McLure R. J., Dunlop J. S., Avison A., 2022,
   MNRAS, 510, 5088
Brammer G. B. et al., 2012, ApJS, 200, 13
Broussard A. et al., 2019, ApJ, 873, 74
Bullock J. S., Dekel A., Kolatt T. S., Kravtsov A. V., Klypin A. A., Porciani
    C., Primack J. R., 2001, ApJ, 555, 240
Calzetti D., Armus L., Bohlin R. C., Kinney A. L., Koornneef J., Storchi-
    Bergmann T., 2000, ApJ, 533, 682
Calzetti D., Kinney A. L., Storchi-Bergmann T., 1994, ApJ, 429, 582
Caon N., Capaccioli M., D'Onofrio M., 1993, MNRAS, 265, 1013
Carnall A. C., McLure R. J., Dunlop J. S., Davé R., 2018, MNRAS, 480,
   4379
Casali M. et al., 2007, A&A, 467, 777
Casey C. M. et al., 2023, ApJ, 954, 31
Casteels K. R. V. et al., 2014, MNRAS, 445, 1157
Ceverino D., Klessen R. S., Glover S. C. O., 2018, MNRAS, 480, 4842
Chabrier G., 2003, PASP, 115, 763
Cheng C. et al., 2020, MNRAS, 499, 5241
Ciesla L. et al., 2024, A&A, 686, A128
Ciotti L., Bertin G., 1999, A&A, 352, 447
Cochrane R. K. et al., 2021, MNRAS, 503, 2622
Cochrane R. K., Best P. N., Sobral D., Smail I., Geach J. E., Stott J. P., Wake
   D. A., 2018, MNRAS, 475, 3730
Cochrane R. K., Best P. N., Sobral D., Smail I., Wake D. A., Stott J. P., Geach
   J. E., 2017, MNRAS, 469, 2913
Conselice C. J., 2014, ARA&A, 52, 291
Costantin L. et al., 2023, ApJ, 946, 71
Covelo-Paz A. et al., 2025, A&A, 694, A178
Crain R. A. et al., 2015, MNRAS, 450, 1937
Cutler S. E. et al., 2022, ApJ, 925, 34
Daddi E. et al., 2005, ApJ, 626, 680
Dalmasso N. et al., 2024, MNRAS, 533, 4472
Davari R., Ho L. C., Peng C. Y., Huang S., 2014, ApJ, 787, 69
Davé R., Anglés-Alcázar D., Narayanan D., Li Q., Rafieferantsoa M. H.,
    Appleby S., 2019, MNRAS, 486, 2827
de Vaucouleurs G., 1948, Ann. Astrophys., 11, 247
Dekel A., Burkert A., 2014, MNRAS, 438, 1870
Dressler A. et al., 2023, ApJ, 947, L27
Dressler A. et al., 2024, ApJ, 964, 150
Duan Q. et al., 2025, MNRAS, 540, 774
Dullo B. T., Graham A. W., Knapen J. H., 2017, MNRAS, 471, 2321
Duncan K. et al., 2019, ApJ, 876, 110
Duncan K. J. et al., 2025, MNRAS, 541, 1329
Dunlop J. S. et al., 2017, MNRAS, 466, 861
Dutton A. A., 2009, MNRAS, 396, 121
Dutton A. A., Van Den Bosch F. C., Dekel A., Courteau S., 2007, ApJ, 654,
Eisenstein D. J. et al., 2023, Overview of the JWST Advanced Deep
   Extragalactic Survey (JADES), preprint (arXiv:2306.02465)
Ekström S. et al., 2012, A&A, 537, A146
El-Badry K., Wetzel A., Geha M., Hopkins P. F., Kereš D., Chan T. K.,
    Faucher-Giguère C.-A., 2016, ApJ, 820, 131
Eldridge J. J., Stanway E. R., Xiao L., McClelland L. a. S., Taylor G., Ng M.,
   Greis S. M. L., Bray J. C., 2017, PASA, 34, e058
Ellison S. L., Sánchez S. F., Ibarra-Medel H., Antonio B., Mendel J. T.,
   Barrera-Ballesteros J., 2018, MNRAS, 474, 2039
Endsley R. et al., 2024, MNRAS, 533, 1111
Endsley R., Chisholm J., Stark D. P., Topping M. W., Whitler L., 2025, ApJ,
```

Endsley R., Stark D. P., Chevallard J., Charlot S., 2020, MNRAS, 500, 5229

Erb D. K., Steidel C. C., Shapley A. E., Pettini M., Reddy N. A., Adelberger

Faisst A. L., Carollo C. M., Capak P. L., Tacchella S., Renzini A., Ilbert O.,

Feng Y., Di-Matteo T., Croft R. A., Bird S., Battaglia N., Wilkins S., 2016,

McCracken H. J., Scoville N. Z., 2017, ApJ, 839, 71

Fan X., Carilli C. L., Keating B., 2006, ARA&A, 44, 415

K. L., 2006, ApJ, 647, 128

MNRAS, 455, 2778

<sup>&</sup>lt;sup>9</sup>https://mast.stsci.ed

```
Ferland G. J., Chatzikos M., Guzman F., Lykins M. L., Badnell N. R., Keenan
   F. P., Porter R. L., Stancil P. C., 2017, Rev. Mex. Astron. Astrofís., 58,
Finkelstein S. L. et al., 2023, ApJ, 946, L13
Freeman K. C., 1970, ApJ, 160, 811
Fu J., Guo Q., Kauffmann G., Krumholz M. R., 2010, MNRAS, 409, 515
Furlanetto S. R., Mirocha J., 2022, MNRAS, 511, 3895
Gardner J. P. et al., 2006, Space Sci. Rev., 123, 485
Garn T. et al., 2010, MNRAS, 402, 2017
Geach J. E., Smail I., Best P. N., Kurk J., Casali M., Ivison R. J., Coppin K.,
   2008, MNRAS, 388, 1473
Giavalisco M. et al., 2004, ApJ, 600, L93
Graham A. W., Driver S. P., 2005, Publ. Astron. Soc. Aust., 22, 118
Graus A. S. et al., 2019, MNRAS, 490, 1186
Grogin N. A. et al., 2011, ApJS, 197, 35
Gruppioni C. et al., 2020, A&A, 643, A8
Guo Y. et al., 2009, MNRAS, 398, 1129
Hao J., Kubo J. M., Feldmann R., Annis J., Johnston D. E., Lin H., McKay
   T. A., 2011a, ApJ, 740, 39
Hao C.-N., Kennicutt R. C., Johnson B. D., Calzetti D., Dale D. A., Moustakas
   J., 2011b, ApJ, 741, 124
Harikane Y., Nakajima K., Ouchi M., Umeda H., Isobe Y., Ono Y., Xu Y.,
   Zhang Y., 2023, ApJ, 960, 56
Harris C. R. et al., 2020, Nature, 585, 357
Harshan A. et al., 2024, MNRAS, 532, 1112
Häußler B. et al., 2007, ApJS, 172, 615
Häußler B. et al., 2013, MNRAS, 430, 330
Hopkins P. F., Kereš D., Oñorbe J., Faucher-Giguère C.-A., Quataert E.,
   Murray N., Bullock J. S., 2014, MNRAS, 445, 581
Hunter J. D., 2007, Comput. Sci. Eng., 9, 90
Huško F., Lacey C. G., Baugh C. M., 2022, MNRAS, 509, 5918
Ito K. et al., 2023, ApJ, 945, L9
Ito K. et al., 2024, ApJ, 964, 192
Ji Z. et al., 2024a, ApJ, preprint (arXiv:2401.00934)
Ji Z. et al., 2024b, ApJ, 974, 135
Jia C. et al., 2024, ApJ, 977, 165
Kannan R. et al., 2025, Open J. Astrophys., 8, 153
Kannan R., Garaldi E., Smith A., Pakmor R., Springel V., Vogelsberger M.,
   Hernquist L., 2022, MNRAS, 511, 4005
Kartaltepe J. S. et al., 2023, ApJ, 946, L15
Katz H. et al., 2023, Open J. Astrophys., 6, 44
Kawamata R., Ishigaki M., Shimasaku K., Oguri M., Ouchi M., 2015, ApJ,
   804, 103
Kelvin L. S. et al., 2012, MNRAS, 421, 1007
Kennicutt R. C., 1998, ARA&A, 36, 189
Kennicutt R. C., Evans N. J., 2012, ARA&A, 50, 531
Kimm T., Cen R., 2014, ApJ, 788, 121
Kocevski D. D. et al., 2025, ApJ, 986, 126
Koekemoer A. M. et al., 2011, ApJS, 197, 36
Labbé I. et al., 2013, ApJ, 777, L19
Lange R. et al., 2015, MNRAS, 447, 2603
Lapiner S. et al., 2023, MNRAS, 522, 4515
Le Fevre O. et al., 2000, MNRAS, 311, 565
Leja J., Carnall A. C., Johnson B. D., Conroy C., Speagle J. S., 2019, ApJ,
   876, 3
Li J. et al., 2024, ApJ, 976, 70
Lin L. et al., 2008, ApJ, 681, 232
Looser T. J. et al., 2025, A&A, 697, A88
Lovell C. C., Vijayan A. P., Thomas P. A., Wilkins S. M., Barnes D. J.,
   Irodotou D., Roper W., 2020, MNRAS, 500, 2127
Ma X. et al., 2018, MNRAS, 477, 219
Madau P., Dickinson M., 2014, ARA&A, 52, 415
Marshall M. A., Wilkins S., Di Matteo T., Roper W. J., Vijayan A. P., Ni Y.,
   Feng Y., Croft R. A. C., 2022, MNRAS, 511, 5475
Martorano M., Van Der Wel A., Baes M., Bell E. F., Brammer G., Franx M.,
   Nersesian A., 2024, ApJ, 972, 134
```

Matharu J. et al., 2022, ApJ, 937, 16

Matharu J. et al., 2023, ApJ, 949, L11

```
Matharu J. et al., 2024, A&A, 690, A64
McClymont W. et al., 2025a, MNRAS, preprint (arXiv:2503.00106)
McClymont W. et al., 2025b, MNRAS, preprint (arXiv:2503.04894)
Meert A., Vikram V., Bernardi M., 2013, MNRAS, 433, 1344
Mercado F. J. et al., 2021, MNRAS, 501, 5121
Mihos J. C., Hernquist L., 1994, ApJ, 425, L13
Miller T. B. et al., 2025, ApJ, 988, 196
Mo H. J., Mao S., White S. D. M., 1998, MNRAS, 295, 319
Moorwood A. F. M., van der Werf P. P., Cuby J. G., Oliva E., 2000, A&A,
   362.9
Morishita T. et al., 2024, ApJ, 963, 9
Mosleh M. et al., 2012, ApJ, 756, L12
Mosleh M., Williams R. J., Franx M., 2013, ApJ, 777, 117
Mowla L., Wel A. V. D., Dokkum P. V., Miller T. B., 2019a, ApJ, 872, L13
Mowla L. A. et al., 2019b, ApJ, 880, 57
Mundy C. J., Conselice C. J., Duncan K. J., Almaini O., Häußler B., Hartley
   W. G., 2017, MNRAS, 470, 3507
Murphy E. J. et al., 2011, ApJ, 737, 67
Naab T., Johansson P. H., Ostriker J. P., 2009, ApJ, 699, L178
Naufal A., Koyama Y., Shimakawa R., Kodama T., 2023, ApJ, 958, 170
Nedkova K. V. et al., 2021, MNRAS, 506, 928
Nedkova K. V. et al., 2024, ApJ, 970, 188
Nelson D. et al., 2019, MNRAS, 490, 3234
Nelson E. et al., 2024, ApJ, 976, L27
Nelson E. J. et al., 2012, ApJ, 747, L28
Nelson E. J. et al., 2013, ApJ, 763, L16
Nelson E. J. et al., 2016, ApJ, 828, 27
O'Leary J. A., Moster B. P., Naab T., Somerville R. S., 2021, MNRAS, 501,
Oesch P. A., Bouwens R. J., Illingworth G. D., Labbé I., Stefanon M., 2018,
   ApJ, 855, 105
Oke J. B., Gunn J. E., 1983, ApJ, 266, 713
Oliphant T. E., 2007, Comput. Sci. Eng., 9, 10
Ono Y. et al., 2023, ApJ, 951, 72
Ono Y. et al., 2024, PASJ, 76, 219
Ono Y., Ouchi M., Harikane Y., Yajima H., Nakajima K., Fujimoto S., Nakane
   M., Xu Y., 2025, ApJ, 991, 222
Ormerod K. et al., 2023, MNRAS, 527, 6110
Oteo I., Sobral D., Ivison R. J., Smail I., Best P. N., Cepa J., Pérez-García A.
   M., 2015, MNRAS, 452, 2018
Ownsworth J. R., Conselice C. J., Mortlock A., Hartley W. G., Almaini O.,
   Duncan K., Mundy C. J., 2014, MNRAS, 445, 2198
Pandya V. et al., 2024, ApJ, 963, 54
Patton D. R., Pritchet C. J., Yee H. K. C., Ellingson E., Carlberg R. G., 1997,
   ApJ, 475, 29
Paulino-Afonso A., Sobral D., Buitrago F., Afonso J., 2017, MNRAS, 465,
Peng C. Y., Ho L. C., Impey C. D., Rix H.-W., 2002, AJ, 124, 266
Peng C. Y., Ho L. C., Impey C. D., Rix H.-W., 2010, AJ, 139, 2097
Perrin M. D., Sivaramakrishnan A., Lajoie C.-P., Elliott E., Pueyo L.,
   Ravindranath S., Albert L., 2014, in Oschmann J. M., Jr, Clampin M.,
   Fazio G. G., MacEwen H. A., eds, Proc. SPIE Conf. Ser. Vol. 9143, Space
   Telescopes and Instrumentation 2014: Optical, Infrared, and Millimeter
   Wave. SPIE, Bellingham, p. 91433X
Pirie C. A. et al., 2025, MNRAS, 541, 1348
Puskás D. et al., 2025, MNRAS, 540, 2146
Qu Y. et al., 2017, MNRAS, 464, 1659
Reddy N. A. et al., 2020, ApJ, 902, 123
Reddy N. A. et al., 2025, The JWST/AURORA Survey: Multiple Balmer and
   Paschen Emission Lines for Individual Star-forming Galaxies at z=1.5-
   4.4. I. A Diversity of Nebular Attenuation Curves and Evidence for Non-
   Unity Dust Covering Fractions, preprint (arXiv:2506.17396)
Rigby J. et al., 2023, PASP, 135, 048001
```

Roberts-Borsani G. W. et al., 2016, ApJ, 823, 143

Roper W. J., Lovell C. C., Vijayan A. P., Marshall M. A., Irodotou D., Kuusisto

J. K., Thomas P. A., Wilkins S. M., 2022, MNRAS, 514, 1921

Robertson B. E. et al., 2013, ApJ, 768, 71

Salim S. et al., 2007, ApJS, 173, 267

Salim S., Boquien M., Lee J. C., 2018, ApJ, 859, 11 Sánchez S. F., 2020, ARA&A, 58, 99 Sanders R. L. et al., 2025, ApJ, 989, 209 Schinnerer E., Leroy A., 2024, ARA&A, 62, 369 Schönrich R., Binney J., 2009, MNRAS, 396, 203 Scoville N. et al., 2007a, ApJS, 172, 1 Scoville N. et al., 2007b, ApJS, 172, 38 Sérsic J. L., 1963, Bol. Asoc. Argentina Astron. La l Sérsic J. L., 1968, Atlas de Galaxias Australes. Ob-

 Sérsic J. L., 1963, Bol. Asoc. Argentina Astron. La Plata Argentina, 6, 41
 Sérsic J. L., 1968, Atlas de Galaxias Australes. Observatorio Astronómico, Córdoba, Argentina

Shen L. et al., 2023, ApJ, 950, 7

Shen X. et al., 2024a, MNRAS, 534, 1433

Shen L. et al., 2024b, ApJ, 963, L49

Shen S., Mo H. J., White S. D. M., Blanton M. R., Kauffmann G., Voges W., Brinkmann J., Csabai I., 2003, MNRAS, 343, 978

Shibuya T., Ouchi M., Harikane Y., 2015, ApJS, 219, 15

Skelton R. E. et al., 2014, ApJS, 214, 24

Smit R. et al., 2015, ApJ, 801, 122

Sobral D. et al., 2009, MNRAS, 398, 75

Sobral D., Best P. N., Geach J. E., Smail I., Cirasuolo M., Garn T., Dalton G. B., Kurk J., 2010, MNRAS, 404, 1551

Sobral D., Best P. N., Matsuda Y., Smail I., Geach J. E., Cirasuolo M., 2012, MNRAS, 420, 1926

Sobral D., Kohn S. A., Best P. N., Smail I., Harrison C. M., Stott J., Calhau J., Matthee J., 2016, MNRAS, 457, 1739

Sobral D., Smail I., Best P. N., Geach J. E., Matsuda Y., Stott J. P., Cirasuolo M., Kurk J., 2013, MNRAS, 428, 1128

Stanway E. R., Eldridge J. J., 2018, MNRAS, 479, 75

Stefanon M., Bouwens R. J., Labbé I., Illingworth G. D., Oesch P. A., van Dokkum P., Gonzalez V., 2022, ApJ, 927, 48

Stott J. P., Sobral D., Smail I., Bower R., Best P. N., Geach J. E., 2013a, MNRAS, 430, 1158

Stott J. P. et al., 2013b, MNRAS, 436, 1130

Stott J. P., Collins C. A., Burke C., Hamilton-Morris V., Smith G. P., 2011, MNRAS, 414, 445

Stoughton C. et al., 2002, AJ, 123, 485

Suess K. A. et al., 2022, ApJ, 937, L33

Sun W., Ho L. C., Zhuang M.-Y., Ma C., Chen C., Li R., 2024, ApJ, 960, 104
 Swinbank A. M., Sobral D., Smail I., Geach J. E., Best P. N., McCarthy I. G.,
 Crain R. A., Theuns T., 2012a, MNRAS, 426, 935

Swinbank A. M., Smail I., Sobral D., Theuns T., Best P. N., Geach J. E., 2012b, ApJ, 760, 130

Tacchella S. et al., 2015, ApJ, 802, 101

Teplitz H., 2018, HST Proposal, 15647

Terao Y., Spitler L. R., Motohara K., Chen N., 2022, ApJ, 941, 70

Theios R. L., Steidel C. C., Strom A. L., Rudie G. C., Trainor R. F., Reddy N. A., 2019, ApJ, 871, 128 Thompson D., Mannucci F., Beckwith S. V. W., 1996, AJ, 112, 1794 Toomre A., Toomre J., 1972, ApJ, 178, 623 Torrey P. et al., 2019, MNRAS, 484, 5587 Traina A. et al., 2024, A&A, 681, A118 Trujillo I. et al., 2006, ApJ, 650, 18 Trujillo I., Conselice C. J., Bundy K., Cooper M. C., Eisenhardt P., Ellis R. S., 2007, MNRAS, 382, 109 Valentino F. et al., 2023, ApJ, 947, 20 van der Wel A. et al., 2012, ApJS, 203, 24 van der Wel A. et al., 2014, ApJ, 788, 28 van der Wel A. et al., 2024, ApJ, 960, 53 van Dokkum P. G. et al., 2010, ApJ, 709, 1018 Varadaraj R. G. et al., 2024, MNRAS, 533, 3724 Vega-Ferrero J. et al., 2024, ApJ, 961, 51 Vijayan A. P., Lovell C. C., Wilkins S. M., Thomas P. A., Barnes D. J., Irodotou D., Kuusisto J., Roper W. J., 2021, MNRAS, 501, Virtanen P. et al., 2020, Nat. Methods, 17, 261 Walcher J., Groves B., Budavári T., Dale D., 2011, Astrophys. Space Sci., Waller W. H., 1990, PASP, 102, 1217 Wang B. et al., 2024b, ApJ, 969, L13 Wang J.-H., Li Z.-Y., Zhuang M.-Y., Ho L. C., Lai L.-M., 2024a, A&A, 686, Ward E. et al., 2024, ApJ, 962, 176 Westcott L. et al., 2025, ApJ, 983, 121 Wilman D. J. et al., 2020, ApJ, 892, 1 Wisnioski E. et al., 2015, ApJ, 799, 209 Wisnioski E. et al., 2019, ApJ, 886, 124 Wootten A., Thompson A. R., 2009, Proc. IEEE, 97, 1463 Wright E. L., 2006, PASP, 118, 1711 Wu X., Davé R., Tacchella S., Lotz J., 2020, MNRAS, 494, 5636 Wuyts S. et al., 2011, ApJ, 742, 96

# APPENDIX: FREE SÉRSIC VERSUS FIXED SÉRSIC SIZES

Yang L. et al., 2025, COSMOS-Web: Unraveling the Evolution of Galaxy

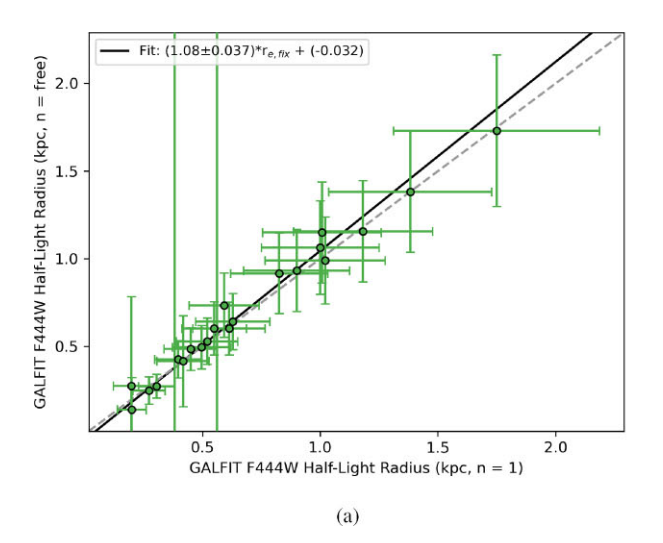
Size and Related Properties at 2 < z < 10, preprint (arXiv:2504.07185)

Wyder T. K. et al., 2005, ApJ, 619, L15

York D. G. et al., 2000, AJ, 120, 1579

Zavala J. A. et al., 2023, ApJ, 943, L9

Zolotov A. et al., 2015, MNRAS, 450, 2327



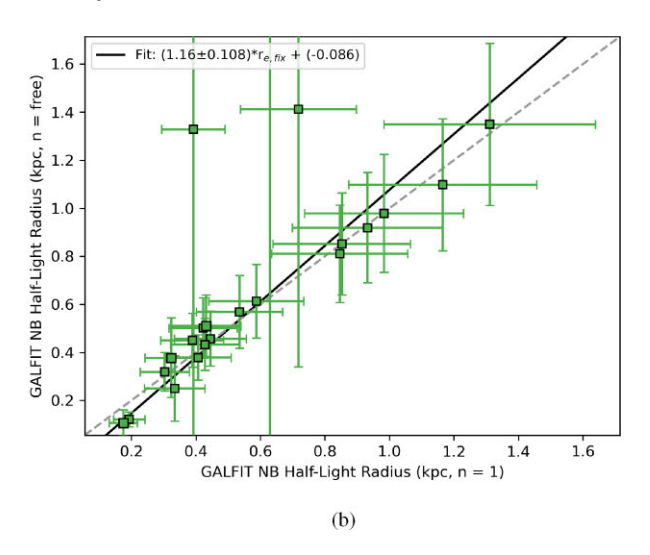


Figure A1. Left: the measured free Sérsic  $r_e$  against fixed n=1 Sérsic  $r_e$  in the F444W observations for each of the HAEs in our sample at z=6.1. Right: same as the left panel, but for the NB observations. The grey dashed line indicates where the  $r_e$  would be equal. The solid black lines show the best fit to the data.

This paper has been typeset from a  $T_EX/I = T_EX$  file prepared by the author.